Validation of Kestrel IDDES Simulations for SLS Transition Analysis

Brent W. Pomeroy[*] and Steven E. Krist[†]
NASA Langley Research Center, Hampton, VA, 23681

Complex computational simulations are required to support the Space Launch System (SLS) program, and the fidelity of the computational results must be defensible. More specifically, a number of databases are produced for the transition phase of flight, which occurs after the rocket clears the launch tower but before reaching transonic speeds. In an effort to reduce computational uncertainty, many of the computational parameters were analyzed to determine the sensitivity of the results to the value of the parameter and then updating the best practice procedures. The baseline routines were developed over many years through the maturation of the SLS program, and this paper delivers a detailed discussion of these baseline results. This section is followed by demonstration of perturbing some of the more significant parameters, including time step and turbulence model, and concluded with a summary of the currently held best practices for such analysis.

Nomenclature

a	=	distance for reference body grid
C_f	=	skin friction coefficient
C_p	=	pressure coefficient
dt	=	time step, sec.
L	=	vehicle height, inches
M	=	Mach number
n	=	an integer number
Q	=	Q-criterion $Q \equiv \left(|\omega|^2 - |S|^2 \right)/2$
Re	=	Reynolds number
S	=	rate of strain, sec^{-1}
$sec.$	=	seconds
t	=	time, sec
x	=	Cartesian coordinate parallel longitudinal centerbody axis
y	=	Cartesian coordinate orthogonal to freestream flow pointed towards the right SRB
y^+	=	nondimensional wall distance
z	=	Cartesian coordinate orthogonal to freestream flow orthogonal to the two SRBs (completes right-hand rule)
α_T	=	angle of attack, deg.
Δ	=	a difference
ϵ	=	a non-integer number
ϕ	=	circumferential angle on the SLS surface, deg.
ω	=	vorticity

14×22	=	NASA Langley Research Center 14- by 22-Foot Subsonic Tunnel
CFD	=	Computational Fluid Dynamics
DOD	=	Department of Defense
HPCMP	=	High Performance Computing Modernization Program
IDDES	=	Improved Delayed Detached Eddy Simulation
KCFD	=	Kestrel Computational Fluid Dynamics
LaRC	=	NASA Langley Research Center
LVSA	=	Launch Vehicle Stage Adapter
NASA	=	National Aeronautics and Space Administration

PSP	=	Pressure Sensitive Paint
QCR	=	Quadratic Constitutive Relations
RANS	=	Reynolds-averaged Navier-Stokes equations
RC	=	Rotation Correction
SA	=	Spalart-Allmaras Turbulence Model
SLS	=	Space Launch System
SRB	=	Solid Rocket Booster
SST	=	Shear Stress Transport

Subscripts
avgstart	=	start of time-averaging window
j	=	index number
ref	=	reference value
t	=	total
∞	=	freestream conditions

I. Introduction

The NASA Artemis program is a large-scale effort that seeks to lead humans into manned, deep-space exploration. Most of the Artemis program is led by NASA with contributors from 15 unique NASA sites. In addition to NASA, some program support is provided through key NASA/industry partnerships and international organizations. One planned step is to construct Gateway, a small space station that will orbit the Moon and facilitate exploration of the lunar surface by both astronauts and autonomous vehicles. Numerous missions, both crew and cargo, are planned to develop the infrastructure and equipment to transport individuals to the station and furnish sustained manned presence on the Moon. A family of heavy-lift vehicles, the Space Launch System (SLS), is currently under development to meet the mission requirements and transportation demands of this program.
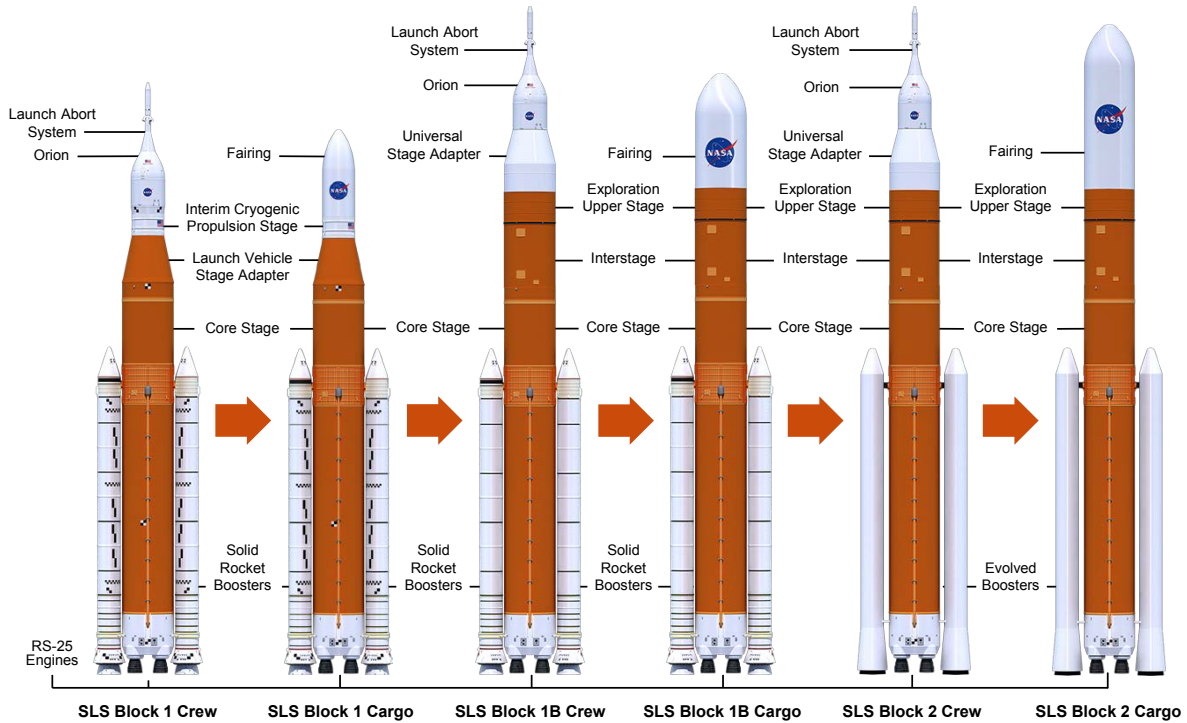
A. Space Launch System

The SLS is a central element of the Artemis program that will provide the capabilities required for manned deep-space exploration. As currently planned, this family of heavy-lift vehicles will enable exploration of the Moon and Mars [1–4]. Three classes of the SLS configuration, each of which includes both a crew and cargo version, are shown in Fig. 1. The large propulsive force needed to propel the targeted payloads is provided by two solid rocket boosters (SRB) side-mounted onto a centerbody that embodies four RS-25 engines. The centerbody is defined as the entire orange core stage, Launch Vehicle Stage Adapter (LVSA), upper stage, and cargo fairing or capsule. Containing a common centerbody, a number of stacks hold the fuel for the RS-25 engines that produce a total of 1.7 million pounds of thrust. A large cryogenic liquid hydrogen tank is located at the base of the centerbody while a cryogenic liquid oxygen tank is located near the top of the centerbody. Mounted on the side of the centerbody, two five-segment, single-use SRBs each yield approximately 3.6 million pounds of thrust such that the desired mission profile can be achieved. The payload, whether the Orion crew capsule or a cargo compartment, is mounted atop the centerbody.

Throughout the course of a mission, the SLS is exposed to a wide variety of flight regimes through the mission profile. While on the launch pad and during the early portions of liftoff, the rocket is subjected to low-speed flow with ground winds from any direction. Upon clearing the tower, the vehicle enters the transition phase of flight with low subsonic Mach numbers and large total angles of attack (α_T). Ultimately, the rocket leaves the transition phase and enters the ascent phase in which it experiences subsonic, transonic, and high supersonic flight regimes. Jettison of the SRBs followed by jettison of the Launch Abort System both occur at the end of the ascent phase of flight. The work in this paper is focused upon the transition flight regime shortly after the rocket clears the launch pad.

B. Aerodynamic Data

Aerodynamic support for the SLS requires the use of both wind tunnel tests and computational simulations to develop aerodynamic databases across the flight mission profile. Due to the wide range of flight conditions experienced during the trajectory of a flight, numerous tools are required to accurately capture the properties of the complex flowfields that evolve over time. Experimental results, which are useful and necessary, are essential to the construction of the databases and validation of computational results. These computational simulations yield results at flight conditions not easily

Fig. 1 Six vehicles in the Space Launch System family including three sizes of rockets with both crew and cargo versions.

tested in a wind tunnel facility. In addition, the computational flowfield can be easily interrogated on the surface and in the volume, thus revealing fine-scale details that are not measurable, or at least not easily measured, in a wind tunnel.

Databases of aerodynamic forces and moments acting on the vehicle throughout the flight regime are provided to a number of different SLS subteams, with the most prominent being the Loads and Guidance, Navigation, and Control groups. While integrated forces and moments on the different components of the vehicle are captured in both computations and experiments, it is not easy to measure distributed loads in an experimental environment. The longitudinal load distribution, referred to as the lineload, is of particular interest [5–12]. While complex and time-intensive experimental pressure sensitive paint (PSP) experiments can be performed, these measurements do not capture skin friction coefficients (C_f), which are a contributing factor to the lineloads. Due to the time required and limitations of PSP experiments, computational simulations serve a vital purpose to generate these lineloads.

C. Transition Flight Regime

The verification and validation exercise discussed in this paper was performed with the Block 1 Cargo vehicle in the transition portion of the mission profile, which is the phase of flight after the rocket clears the tower but before ascent begins. During transition, the total angle of attack (α_T) ranges from nearly 90 deg. at the beginning of the phase through nearly 0 deg. at the end of the phase. The roll angle during liftoff and transition ranges from 0 to 360 deg. At the moderate to large α_T usually experienced during transition ($\alpha_T > 20$ deg.), significant separation is observed on the leeward side of the rocket. The wake in this region is extremely unsteady, and the large-scale separation dominates the flowfield. Due to the complex flowfield, it can be difficult to accurately capture this wake using computational methods using traditional computational schemes.

Vehicles with slender forebodies, such as the SLS, can generate two large, stable asymmetric vortices at moderate to high α_T, as extensively documented in the literature [5–7, 13–16]. Typically, the vortex on one side of the body will be small and stay close to the body while the opposite vortex will be larger and further off the surface, as seen in Fig. 2. Both primary vortices may generate a secondary vortex, also shown in the figure. Despite the unsteady nature of the wake over part of the rocket, these vortices vary little with time. Because of the asymmetric nature of
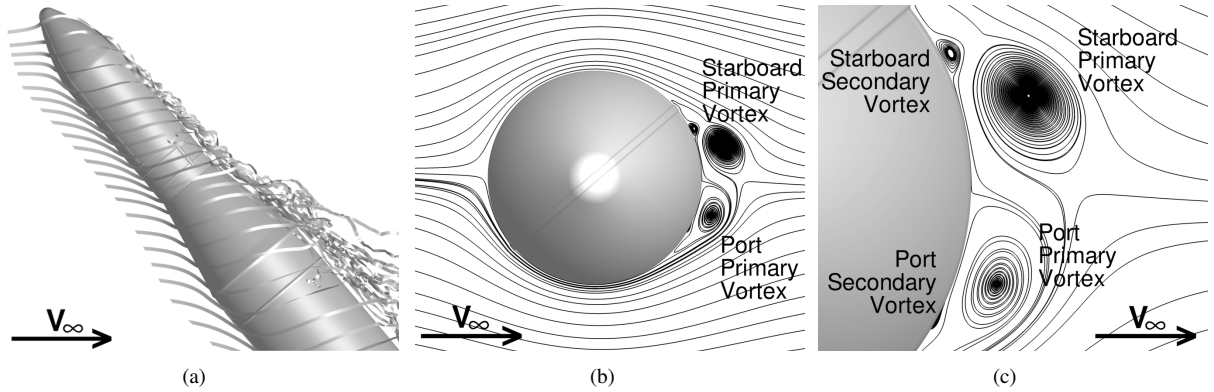
Fig. 2   Separated flowfield showing primary and secondary asymmetric vortices in a) profile, b) top down (wide), and c) top down (zoomed) views.

the flowfield, a significant side force may be exerted on the body. To further complicate the situation, it is noted that this asymmetric vortex may switch from side to side of the body at different instances of the same condition. With increased downstream distance, the vortices will break down into a massively-separated flowfield. The point at which a vortex bursts is dependent on many factors including freestream conditions, the quality of the construction of the vehicle or model, and the fidelity of the computational simulation. Even with high-fidelity computational solvers, it can be extremely difficult to accurately predict the asymmetric vortex as a stable state exists with the largest vortex on both sides of the slender body. As visualized in Fig. 2(b,c), a seam is present on the upper stage. This feature causes flow separation at a specific flight condition, which results in a large primary vortex on the starboard side of the vehicle at no roll angle. This seam does not exist on the other configurations. Consequently, as only one stable mode exists for the Block 1 Cargo vehicle at this roll angle, this configuration was selected for the detailed verification computational study.

While the asymmetric vortices can dominate the flowfield at these moderate to large angles of attack, the Coandă effect is most prominent at high angles of attack. In addition to the large-scale separation, the flowfield exhibits the Coandă effect, which is the tendency for the flow emanating from a jet to remain attached to a curved surface. For the SLS, the Coandă effect is a function of the gap size between the SRBs and centerbody and also the diameter of the two bodies [5, 6, 17, 18]. With slight changes in freestream condition or geometry, the flow may exhibit different attachment characteristics through the SRB/core gap. Similar to the asymmetric vortices, this feature can be difficult to capture computationally, thus adding to uncertainty of the simulations. For the case at α_T of 90 deg. and roll angle of 0 deg., there are four different Coandă modes, seen in Fig. 3, including:
- flow bends to the left and attaches to the port SRB and centerbody
- flow bends to the right and attaches to the starboard SRB and centerbody
- flow bends around, and attaches to neither SRB and both sides of the centerbody
- flow bends around, and attaches to both SRBs and neither side of the centerbody
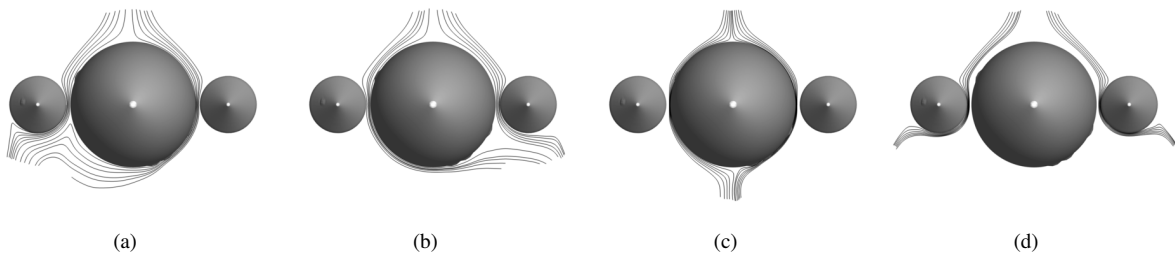
Fig. 3   Four different Coandă modes depicting flow attached to a) the port SRB and centerbody, b) the starboard SRB and centerbody, c) the centerbody, and d) both SRBs.

II. Block 1 Cargo Vehicle

While the SLS family is comprised of six unique vehicles, the verification and validation study was focused on the Block 1 Cargo configuration, shown in Fig. 4. This vehicle was selected for a few reasons. First, the geometric simplicity of the cargo forebody relative to the crew geometry was desired. The smooth cargo fairing with seam generates two consistent asymmetric vortices over the forebody and a significant portion of the centerbody. On the crew version, the complex Launch Abort System and Orion capsule yield significant separation instead of the two asymmetric vortices. In addition, the Block 1 model was chosen due to the maturity of the design and existence of significant wind tunnel data. Similar to the vehicle selection, the transition regime was chosen to minimize computational cost and decrease flowfield complexity. Absence of the tower reduces the complex wakes interacting between the vehicle and tower. As a reminder, the centerbody is comprised of the core (lower stage), LVSA, and cargo fairing.
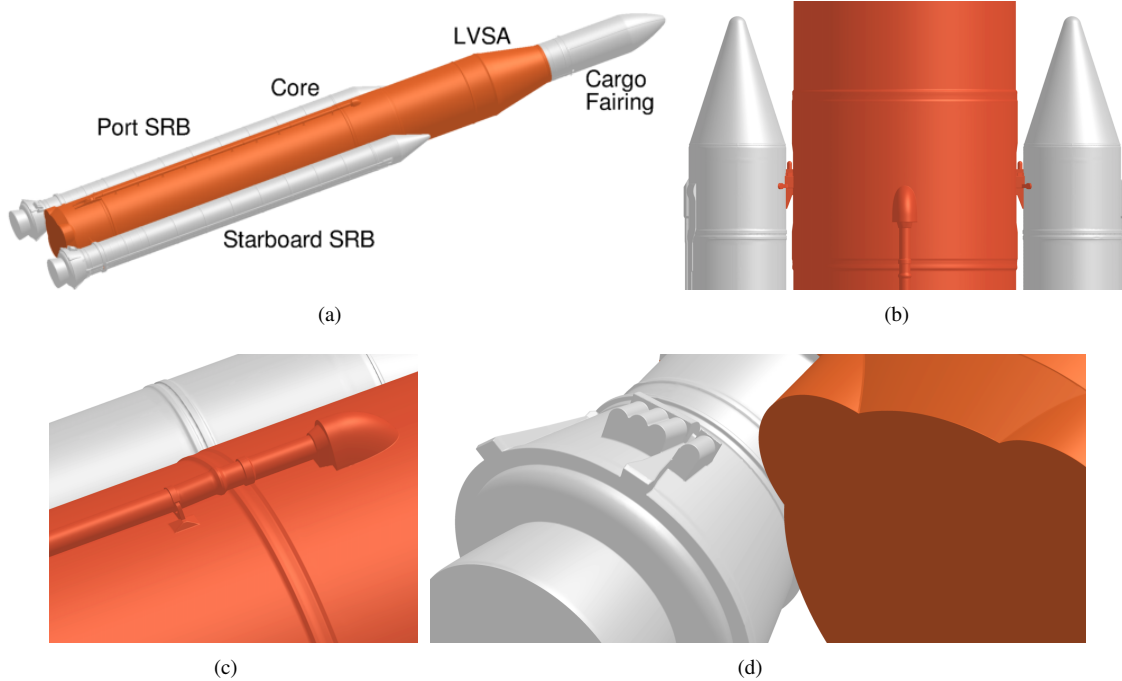
Fig. 4   Block 1 Cargo computational model including a) full vehicle, b) SRB mounting hardware, c) liquid oxygen feed line and circumferential rings, and d) booster separation motors and circumferential rings.

The high-fidelity geometry modeled in the computational simulation, shown in Fig. 4, captures many features of the actual SLS geometry including many small-scale surface protuberances and pieces of hardware. Two sets of mounting brackets, one fore and one aft, connect the SRBs to the centerbody. Each of the liquid oxygen supply lines, a long longitudinal pipe, and associated mounting hardware is accurately modeled. In addition, circumferential rings around the centerbody and SRBs are also modeled appropriately. The booster separation motors are also easily visualized in the figure. In addition to these features, a wide number of other protuberances and surface features were captured. The liquid hydrogen repressurization lines on the bottom side of the centerbody were the only major features not modeled in the computational loft.

The baseline missile-axis SLS coordinate system is defined such that the x axis is pointed down the centerline of the body, y points toward the starboard, or right, solid rocket booster, and the orientation of z completes the right hand rule, shown in Fig. 5. A small black diamond represents the moment reference point for SLS. Also seen in the figure, the freestream velocity approaches the side of the vehicle that contains the systems tunnel. Consequently, for the analysis in this paper, the windward side of the vehicle approaches the systems tunnel while the leeward surface opposes the systems tunnel. Finally, the circumferential location on the rocket is defined by ϕ with the orientation as plotted.
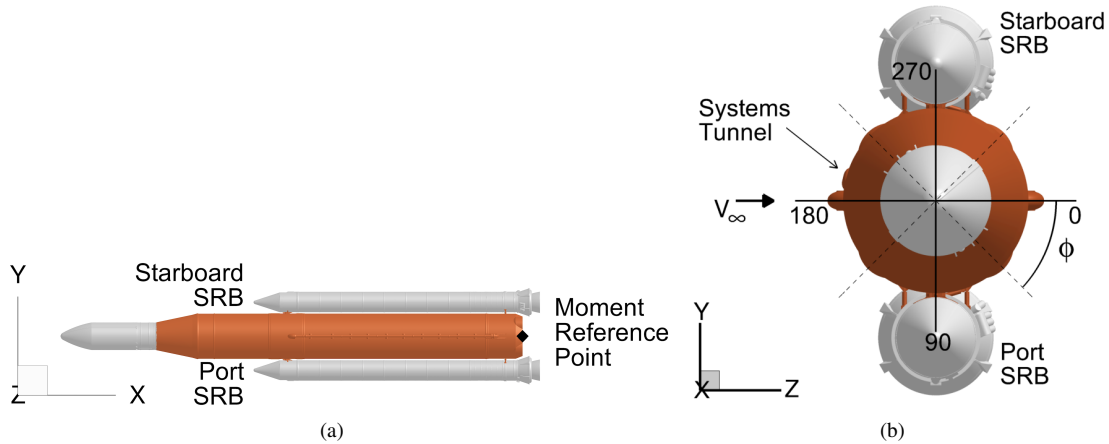
Fig. 5   Coordinate system showing centerbody and SRBs in a) side view and b) front view.

III. Methods

A number of different methods were utilized through the course of this project to acquire the necessary experimental and computational data. Computations were performed using the Kestrel CFD code on the Pleiades supercomputing cluster at the NASA Ames Research Center with unstructured grids generated using Heldenmesh. Experiments were executed in the NASA Langley Research Center (LaRC) 14- by 22-Foot Subsonic Tunnel (14×22). Each of these methods will now be discussed in greater detail.

A. Kestrel

The Kestrel CFD package is a suite of programs that enable solution preparation, adaptive grid generation, computational calculation, and simple postprocessing of both Reynolds-averaged Navier-Stokes (RANS) and Improved Delayed Detached Eddy Simulation (IDDES) schemes [19–22]. Kestrel is developed and maintained by the Computational Research and Engineering Acquisition Tools and Environment, Air Vehicle (CREATE-AV) project and executed by the Department of Defense High Performance Computing Modernization Program (DOD HPCMP). Unless otherwise noted, all simulations in this report were executed with Kestrel 10.3.

The Kestrel Computational Fluid Dynamics flow solver (KCFD) is a finite-volume, cell-centered, unstructured flow solver for both two- and three-dimensional configurations. Solutions can be executed on a variety of cell types including tetrahedra, prisms, pyramids, and hexahedra. Parallel processing is executed by splitting the computational domain into the same number of zones as processors, and a Method of Lines approach is utilized such that the temporal and spatial integration schemes are decoupled from each other. A second-order accurate spatial algorithm is used, and up to a second-order accurate temporal scheme is implemented with a subiteration point-implicit algorithm. A wide number of settings can be used to control the behavior of the computational solver. Some of these values can dramatically affect the fidelity and stability of a solution, so great care must be taken when setting each parameter. A large number of the effects of these settings is examined throughout this paper.

In some cases, it may be necessary to accurately resolve a flowfield exhibiting separation or other complex offbody flowfield features. While a large unstructured grid can be generated, it may be desirable to implement an adaptive mesh routine to yield high-resolution grid where large gradients exist while relaxing the cell size in other portions of the flowfield. If this is selected in Kestrel, a dual-mesh approach, including a static near-body unstructured grid and an adaptive offbody Cartesian grid, is employed. Similar to KCFD, SAMAir, the off-body Cartesian grid solver, is dependent upon a number of parameter values chosen by the user. Unlike the user-generated unstructured grid, both the initial and final Cartesian grid is generated automatically by SAMAir. A trimmed internal unstructured grid is combined with user-specified outer domain limits for the Cartesian grid. The overlap between the two grids and the associated grid density is generated by SAMAir such that the structured and unstructured cell sizes are similar at the edge of the inner grid. Refinement is executed at a user-specified number of iterations for a given maximum cell size, and refinement tracks either the magnitude of vorticity ($|\omega|$) or the Q criterion. Seen in Fig. 6, a refined cell has sides that are one half
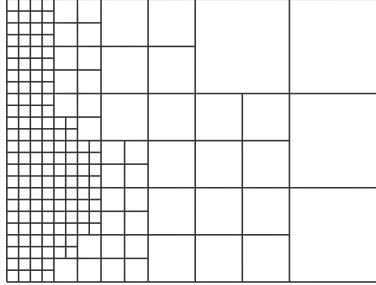
Fig. 6 Schematic of an example Cartesian grid with cell sizes one-half the length of a neighboring, larger cell.

the length, in all three dimensions, of a neighboring, larger cell. Large grids may contain tens of thousands of zones with large differences in cell sizes, so the user must carefully consider the refinement of the inner grid and the size of the computational domain.

B. GridTool

GridTool, a component of the NASA Langley Tetrahedral Unstructured Software System (TetrUSS), was used to prepare the geometry for both grid generation and solution setup [23, 24]. With leverage of automatic geometry programs and significant user interaction, nearly 4,500 patches were used to define the surface outer mold lines. Patches are defined by many different curves that are usually, but not always, coincident with an underlying surface. The boundary condition can be independently selected for each patch.

C. Heldenmesh

Given proper modeling of the SLS surfaces, unstructured grids were generated with the Heldenmesh program. The general approach to developing the surface grid was developed over many years of SLS simulations and associated lessons learned in those efforts within the Configuration Aerodynamics Branch [5, 6, 10, 25]. Heldenmesh is a three-dimensional unstructured grid generator that produces both surface and volume grids that employs the advancing-front and advancing-layers techniques. The viscous grid spacing is defined by

$$\delta_j = \delta_1 \left[1 + R_1 \left(1 + R_2 \right)^{j-1} \right]^{j-1} \tag{1}$$

in which δ defines the cell spacing, j represents a grid index, δ_1 is the user-specified cell height for the first cell, and R defines two growth-rate parameters. As seen Eq. 1, the number of layers for the viscous grid cannot be absolutely specified by the user. However, a target number of layers results in a grid that is close to this value.

D. Computational Resources

All simulations were performed on the NASA Advanced Supercomputing (NAS) facility at the NASA Ames Research Center. The large-scale cluster consists of over 11,000 nodes, more than 241,000 compute cores, and nearly one petabyte of memory in which the cores are connected through InfiniBand with a partial hypercube topology. Unless noted otherwise, all computations were performed on Haswell nodes, and most were executed with 80 Haswell nodes for a total of 1,920 cores. A standard job, in which only limited volume data were saved, took up approximately 600 GB of disk space that was stored on an array of hard disk drives. A select few cases were executed wherein approximately 1,000 unstructured volume solutions were saved over the course of the solution, and these totaled about 6 TB of data.

E. Experimental Facility

Experimental data were collected in the 14×22 in both the liftoff and transition regime with a sting-mounted 1.75% scale model [8, 26–30]. The tunnel is an atmospheric, closed-circuit, low-speed wind tunnel that is used to capture aerodynamic performance of both powered and unpowered aircraft, launch vehicles, and reentry vehicles. The 40-ft diameter fan, powered by a 12,000 horsepower drive motor, facilitates continuous control of the tunnel between Mach 0 and 0.3. The boundary layer is approximately 5 inches thick in the test section, and a boundary layer mitigation system

reduces the size of the boundary layer. The sting-mounted model, nominally in the middle of the tunnel, did not require the boundary layer removal mitigation for this test.

IV. Baseline Solution

Prior to this report, a number of computational databases, and accompanying documentation, have been delivered using a baseline setup for Kestrel [5–7, 10, 29]. A detailed examination of these settings is warranted to understand the governing flowfield and solution behavior. With an adequate understanding of the flowfield, it is possible to evaluate the effect of various input values on the final solution, and the independent effect of time step and turbulence model are discussed later in this report. A detailed investigation of the baseline setup and flowfield follows in this section.

A. Freestream Conditions

Through the course of this study, computational data were compared to wind tunnel results. Consequently, it was necessary to match the freestream conditions in the experimental facility with the reference quantities in Kestrel including Mach number (0.183), freestream Reynolds number (Re) based on a given reference length (L), and static temperature. The Mach number of 0.183 was chosen to accurately match previously-collected wind tunnel data. The freestream Reynolds number is determined from the freestream conditions. It is noted that the liftoff case, in which the rocket is on or near the tower, is subjected to freestream conditions closer to Mach 0.05. This regime is beyond the scope of this report. All data in this section are presented at a total angle of attack (α_T) of 50 deg.

B. Baseline Input File and Settings

The baseline computational setup is similar to those used in previous studies [5, 6, 10]. A wide number of settings can be selected, and the LaRC SLS CFD team collaborated with Scott Morton and David McDaniels of CREATE-AV for guidance regarding the initial selection of these input parameters. Due to program constraints, only a limited study was performed to defend the selection of these parameters in these previous studies. Consequently, a comprehensive examination has been undertaken to quantify the effect of many of these input selections.

An extremely large number of parameters can be selected to control the behavior of the two computational solvers [19, 22]. The baseline case included an IDDES formulation using the one-equation Spalart-Allmaras (SA) turbulence model. While a time-dependent solution will never converge to a single value of a force or moment, these values do fluctuate around a certain mean value after many iterations. This is deemed to be a statistically-steady state. To ensure the integrity of the simulation, it is necessary for the flow solution to set up for a sufficient number of iterations to achieve such a condition. For the baseline solution, a time step of 0.0005 sec. was selected for a total of 14,000 iterations, or 7.0 sec. Time averaging was declared to start at 10,000 iterations (5.0 sec.) and applied over a period of 4,000 iterations (2.0 sec.). For a case at which the rocket is at $\alpha_T = 0$ deg., the characteristic length of the rocket would be L, the length of the vehicle. However, the core diameter is the characteristic length at $\alpha_T = 90$ deg. Consequently, the characteristic length at $\alpha_T = 50$ deg. was taken to be a blending of the rocket length and core diameter. Based on this hybrid value, the flow passed through this characteristic length for multiple times during the time-averaged portion of the solution.

C. Grid

It is widely known that the computational mesh used in a study can have dramatic effect on the accuracy of the simulation. The first-order effect of the grid is large, and the importance cannot be understated. As the Kestrel formulation employed a near-body unstructured grid overlapped with an off-body Cartesian grid, the integrity of both computational grids must be verified. While such a grid study is beyond the scope of this paper, the following section contains an examination of the baseline unstructured and Cartesian grids.

1. Unstructured Grid

The unstructured surface grid was generated in Heldenmesh. A number of source distributions on a variety of patch families were declared, and the grid was made on the geometry as defined in GridTool. A total of 53,516 sources were automatically generated by Heldenmesh, which resulted in 2,290,722 triangular surface cells. The resulting surface grid, including y^+ and volume of the first cell including initial cell height, is visualized in Fig. 7. Following best practices that have been developed in previous studies, a minimum of four cells was desired on every surface, even on detailed

features. Extremely small values of y^+ are present over much of the vehicle with some elevated values resulting near the vortices. Ideally, y^+ would be less than 0.7 at all surface locations. However, elevated y^+ values, even in excess of 1.0, are seen over the SRB nose. Figure 7(b) plots the volume of the first cell over the SLS. It is clear that reduced cell sizes define small-scale features, such as the circumferential rings, with wider spacing specified on the centerbody.

(a)   (b)
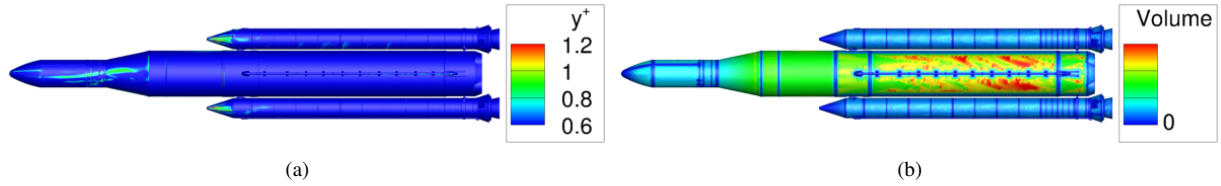
Fig. 7   Unstructured surface grid quantified by a) $y+$ and b) cell volume.

2. Initial Cartesian Grid

As previously mentioned, SAMAir generates a preliminary grid prior to the first iteration. Slices of this grid at constant x and centerline of the body (z=0) are plotted in Fig. 8 in which the mesh is colored by the three-dimensional cell volume. Blue cells depict the smallest cells while red indicates the largest cells. The figure is zoomed to allow detailed viewing of the body. Both the inner and outer grids are shown. The Cartesian grid is comprised of about 315 million cells and nearly 30,000 blocks. As seen in the figure, the interior portion of the structured grid contains similar cell volumes to that of the unstructured mesh. Systematic coarsening of the grid is present with increasing distance from the body. While the inner grid extended approximately $0.11 L_{ref}$ from the surface of the vehicle, the outer grid extended at least $7L$ in all directions relative to the closest point on the vehicle surface where L is the vehicle length.


(a)   (b)
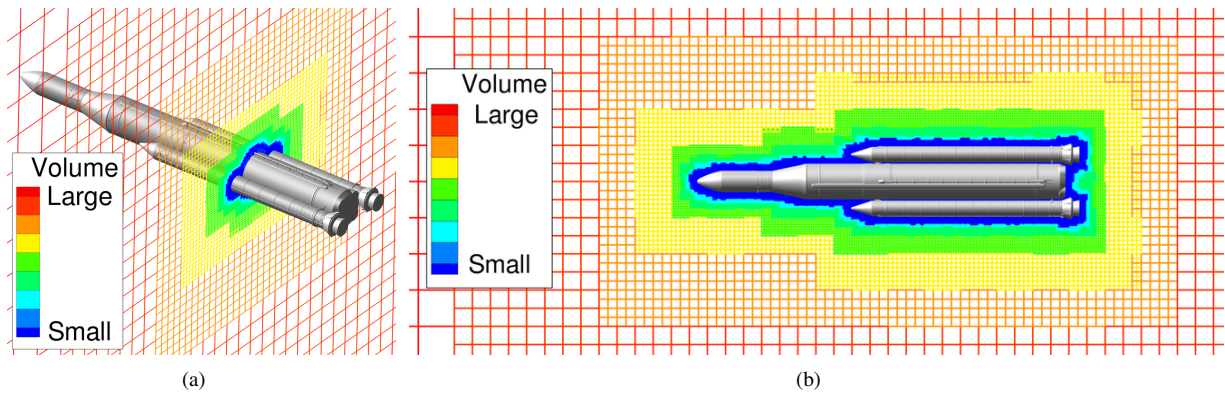
Fig. 8   Zoomed view of the baseline Cartesian grid from SAMAir at beginning of run showing a) constant x and b) constant z.

3. Adaptive Mesh Refinement

The Cartesian grid was refined based on vorticity every 250 iterations after the first 500 iterations for the entire length of the solution. While refinement was applied over the entire simulation, ideally, no significant adaption would be applied to the grid after the start of solution averaging. Figure 9 shows a front view of the vehicle with a slice of the instantaneous solution at 2,000 and 10,000 iterations, the point at which time averaging commenced. The domain is sliced at an x station just downstream of the nozzle exit plane. In the figure, the grid slice is colored by vorticity, $|\omega|$, the parameter that was used to control grid adaptation. The inner, unstructured grid is not displayed in the figure so that it is easier to visualize the extent of the Cartesian grid and associated refinement. In the two figures, the innermost portion of

9

the Cartesian grid has similar refinement at both time steps. However, significant refinement in the wake region resulted in a larger, higher-quality grid that adequately captures the small-scale flow features. Even though this solution was executed at a vehicle roll angle of 0 deg., Fig. 9(b) indicates that the flow is not symmetric about the body centerline. In addition to the separated wake, the complex flowfield also includes the large asymmetric vortices and Coandă effect.

(a)   (b)
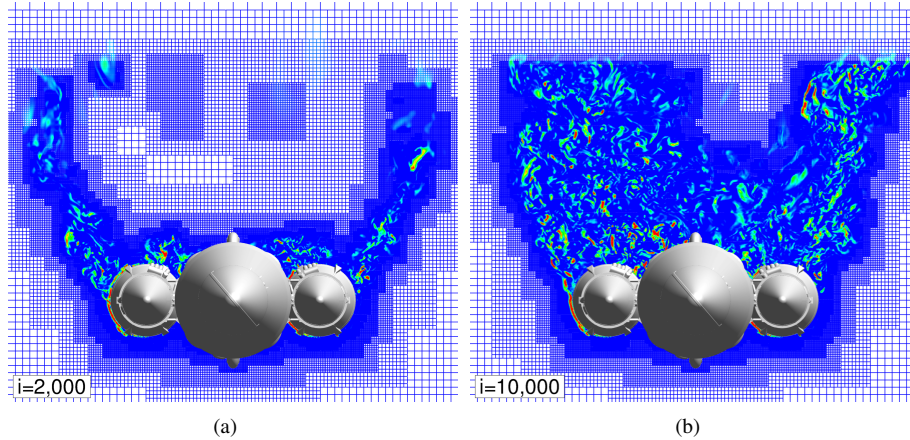
Fig. 9   Front view of instantaneous solution for M=0.183 and α_T=50 deg. for Cartesian mesh at nozzle exit plane colored by $|\omega|$ at a) 2,000 iterations and b) 10,000 iterations.

The initial Cartesian grid was comprised of about 315 million cells distributed through nearly 30,000 blocks. Over the course of the solution, the final outer grid was refined to about 1.5 billion cells in approximately 67,500 blocks. This is an increase by about a factor of five relative to the baseline grid. Results indicate that minimal changes in the grid are applied after iteration 5,000. This brings confidence to the integrity of the solution through the time-averaging portion of the solution in which averaging commences at 10,000 iterations.

D. Convergence

After a solution has completed, it is important to ensure the solution is adequately converged. For an adaptive-grid solver like Kestrel, it is necessary to monitor the size and behavior of the automatically-refined Cartesian grid in addition to solution residual and forces and moments. The convergence of a solution and minimization of the residual is a function of numerous parameters and settings. Without a high-quality inner and outer grid, the solution may diverge or yield an inaccurate solution. Additionally, improper selection of various inputs may also alter the results. Convergence metrics for this baseline solution are plotted in Fig. 10 including the integrated normal and side force coefficients on the centerbody as well as the residual for the entire flowfield. For Figs. 10(a-b), the instantaneous value is plotted as a thin red line while the moving time-averaged value is shown as a thick green line. In these plots, the side and normal forces act along the y and z axes, respectively. As plotted in the figure, the normal and side forces exhibit time dependency, even during the averaging portion of the solution. This is the expected behavior. Ideally, the time-averaged line would be nearly horizontal over the course of the time-averaging window. While the normal force exhibits little variation in this window, differences are observed for the side force. This observation indicates that the flow may not be sufficiently set up and the averaging window may need to begin at a later iteration. The solution residual, plotted in Fig. 10(c), shows some variation in time, but the trends are largely the same after about 5,000 iterations. Finally, the convergence through three subiterations, corresponding to one global time step, is plotted in Fig. 10(d). Data are depicted from subiteration 30,000 to 30,014 which is global iteration 10,000 through 10,004. This plot, which shows the residual of the mass equation, decreases by more than one order of magnitude from 2.4 to approximately 1.0.

E. Time-Averaged Solution

Considering the baseline flowfield to be sufficiently converged, as indicated in Fig. 10, a detailed investigation of the time-averaged solution is warranted. The flowfield at α_T of 50 deg. is shown in Fig. 11 with text labeling key aerodynamic features. Freestream air nominally moves from left to right with a 50 deg. rotation about the y axis and

10
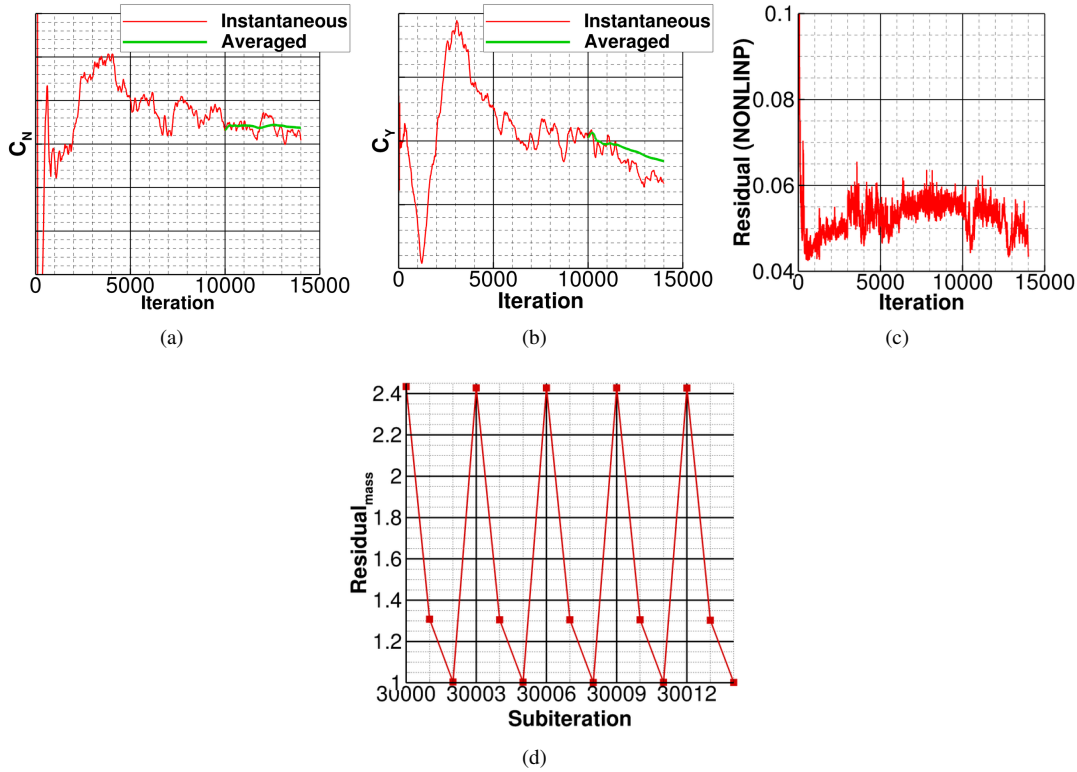
Fig. 10 Flowfield convergence evidenced by a) normal force, b) side force, c) solution residual, and d) subiteration convergence.

no rotation about z. To aid in the visualization of these results, a reference surface grid has been developed. This dimensional body grid depicts reference lines at constant x and y. Thick major grid lines exist every a lengths, and thin minor grid lines are shown every $0.25a$ lengths on the surface of the body. This grid is shown at constant x and y with the same grid spacing in each direction. It is emphasized that this feature is only used to aid in postprocessing and is not the underlying unstructured mesh.

In addition to the reference grid, an isosurface of constant Q is colored by the magnitude of vorticity in which the leeward (suction) side of the surface with the associated large-scale separation is visible to the reader. A number of flowfield features are observed including a pair of asymmetric vortices in addition to a smaller vortex on the far starboard side of the vehicle. These two large vortices originate near the nose of the centerbody, and asymmetry in these features is observed, as highlighted in Fig. 2. The port asymmetric vortex is significantly larger in diameter and length than the starboard vortex. While the starboard vortex bursts approximately $5a$ from the nose, the port vortex extends over the Launch Vehicle Stage Adapter prior to decomposing into separated flow.

A smaller vortex, visualized on the extreme starboard side of the Launch Vehicle Stage Adapter (LVSA), originates at the junction between the upper stage and the LVSA and remains intact until near the SRBs. This vortex exhibits a significant reduction in $|\omega|$ relative to the two asymmetric vortices, thus indicating a decreased strength relative to the vortices near the nose. In addition, two asymmetric vortices are observed over the nose of each SRB. The two SRBs show general topological symmetry with the outboard vortex being larger and stronger than that next to the gap. The larger vortex extends downstream approximately $3a$ prior to breaking down into a separated flowfield.

In addition to the previously-discussed isosurfaces, it can be beneficial to interrogate the flowfield with a number of slices, as shown in Fig. 12. Similar to the reference body grid, a reference polar grid is shown at a number of body stations. In these slices, lines of constant radius and constant ϕ can be seen. Thick lines are plotted every b inches and 30 deg. while thin lines are shown every $0.25b$ inches and 10 deg. An outer radius was chosen to be $2b$ inches to adequately capture the entire unstructured grid, which was trimmed at approximately $1.8b$ from the surface of the vehicle.

11
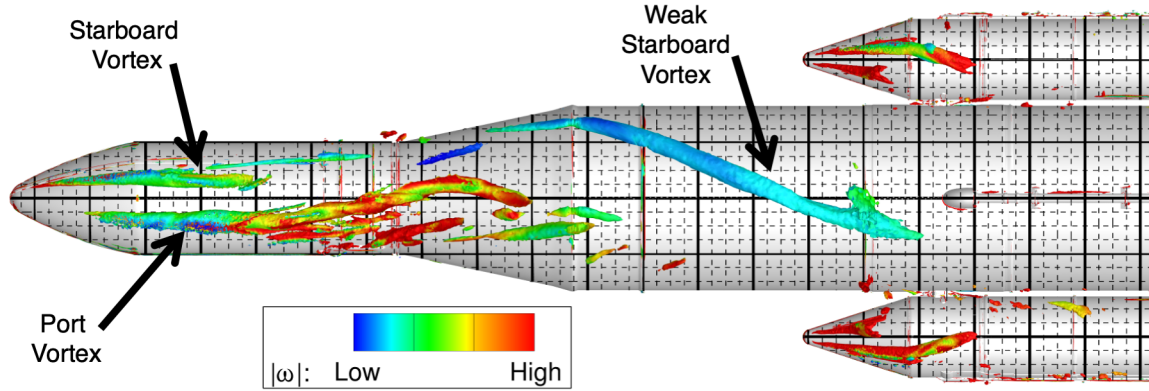
Fig. 11 View of flow over Block 1 Cargo vehicle at α_T of 50 deg. showing isosurface of constant Q colored by $|\omega|$ on the leeward side of the vehicle.

Contours on each of these station cuts show $|\omega|$, the same value that floods the isosurface in Fig. 11. In the figure, blanking was applied for locations in which $C_{p,t} > \epsilon$ and ϵ is close to, but not equal to, 1.0. The total pressure coefficient, $C_{p,t}$ captures the losses of a flowfield in which a value of 0 applies to no momentum (full losses) and 1.0 is the same as freestream momentum (no losses). By selectively blanking a slice, it is easy to visualize the region of separation. The downstream development and decomposition of the two vortices is easily visualized across these three slices. Near the nose, a cross-section of the starboard vortex is nearly circular, but the port vortex is wider than tall in the same region. By the second slice, the starboard vortex has largely decomposed. However, the port vortex exists through all three body slices. On the port side of the second slice, the flow that is being entrained by the vortex is seen to be lifted off the surface, seen in the blue region just outboard of the primary vortex. Careful interrogation of the solution indicates the existence of a secondary vortex, bringing confidence to the computational approach and grid resolution. Without sufficient resolution, it is impossible to capture this secondary vortex. Note that the outer edge of the polar grid is $2b$ from the surface of the body, and the unstructured grid was trimmed about $1.8b$ off the surface. Consequently, flow that appears to be truncated toward the edge of the reference polar corresponds to flow that is in the outer, Cartesian grid. Because adaptive mesh refinement is applied to the Cartesian grid, the vortex is still adequately resolved in the Cartesian grid.
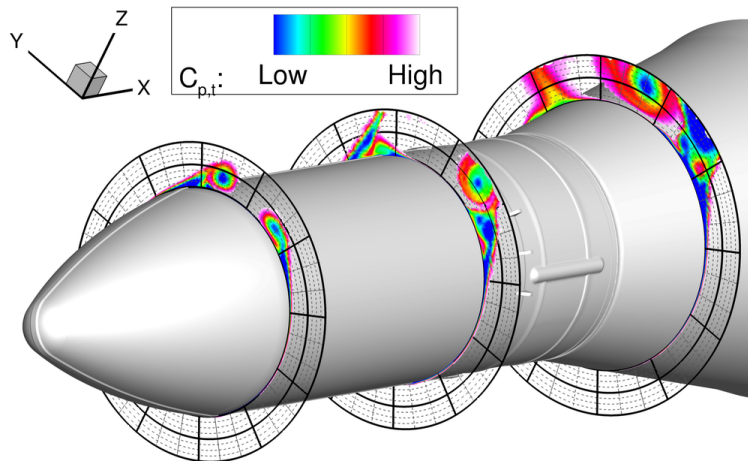
Fig. 12 Body station slices colored by $|\omega|$ at three downstream distances coplotted with reference grid.

The longitudinal load distributions, known as the lineloads, are of critical importance to the program, and these data are one of the major deliverables from the aerodynamics group to other subteams. The two primary metrics of interest are the side force that acts along the y axis and the normal force that acts along the z axis. These load distributions, normalized by reference quantities, on the centerbody are shown in Fig. 13. For reference, the rocket outline is coplotted

with the force distributions. Nonzero values of C_Y over the upper stage and upstream portion of the core is clear evidence of the asymmetric nature of the two upstream vortices. If the vortices exhibited pure symmetry, the side force in the upstream portion of the body would be zero. Relatively smooth side force upstream of the SRBs shows the small-scale turbulence averages to zero in the averaging window. Similar to the side force, the normal force is largely well behaved upstream of the SRBs. A number of peaks in the normal force lineload result from protuberances on the surface (such as circumferential rings, joints, etc.), which cause localized separation. Additionally, the gap flow between the SRBs and centerbody significantly affects the normal force. This highly complex flow includes attached and separated flow regions that occur on the surfaces between the SRBs and the centerbody. Downstream of the SRB nose, the two load distributions are not smooth, which is a result of the massive, large-scale separation over the rocket.
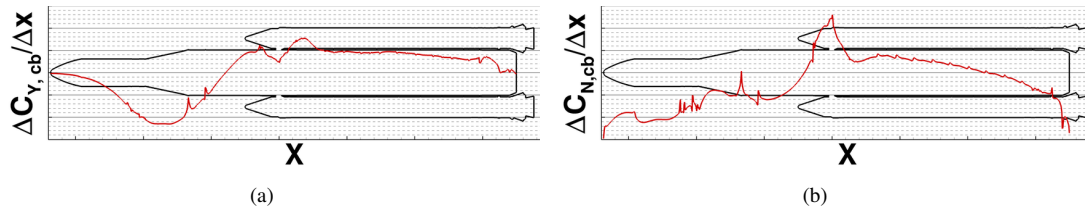
Fig. 13   Centerbody lineloads for baseline solution including a) side force and b) normal force.

F. Unsteady Solution

Plots showing the upper surface at two snapshots in time, at 5.0 sec. and 6.0 sec., are shown in Fig. 14. When comparing the results, both striking similarities, as well as some differences, are observed. First, both snapshots indicate the two asymmetric vortices in the upstream portion of the flowfield with the larger vortex on the port side of the centerbody. Few small-scale turbulent features are observed in this region of the flowfield, indicating the flow is nominally attached to the surface of the vehicle. Even though the boundary layer is entrained into the vortex, the flow is considered to be well behaved as large-scale separation is not present.
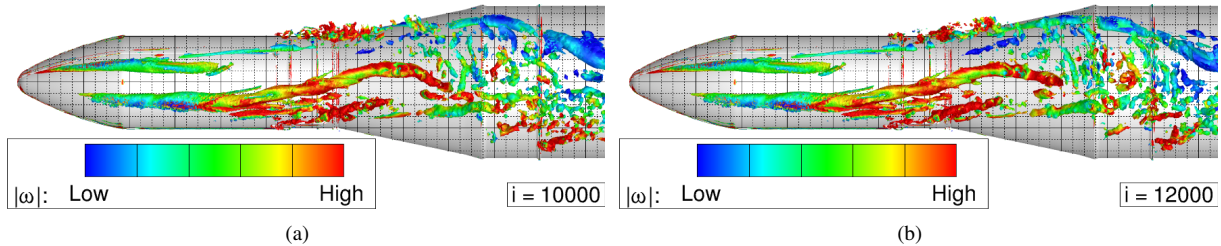

Fig. 14   Instantaneous snapshot in time showing isosurfaces of Q colored by $|\omega|$ at a) 10,000 iterations and b) 12,000 iterations.

Overall, few differences in the asymmetric forebody vortices are observed between the two time steps. These observations indicate that the vortices are stable in time and do not exhibit any transient vortex wandering or vortex bursting. While only two snapshots in time are shown in the figure, this behavior was observed through the entirety of the time-averaged portion of the solution. Further downstream, the asymmetric vortices break down from the well-behaved flowfield into large-scale, broadband separation. When comparing the two plots, some significant differences are observed in this separated region, which is the expected behavior. Even though these turbulent structures are not visible in the time-averaged flowfield, Fig. 14 indicates a significant temporal variation in the separated flowfield. It is observed that the time-averaged solution in Fig. 11 contains the two, large asymmetric forebody vortices and a third, smaller vortex that wraps around the starboard side of the vehicle. While the two asymmetric forebody vortices are clearly visible in Fig. 14, the third vortex is not observed. Consequently, it is concluded that this smaller vortex exhibits significant temporal unsteadiness, in contrast to the stable asymmetric vortices.

Surface pressure data were extracted at five different locations on the surface, and the results are seen in Fig. 15. These five locations, labeled A through E, lie on the maximum value of z for which $y = 0$ at a specified x-station, which is only true if the roll angle is 0 deg. These five points were selected for additional investigation as they included the area in which the flow is attached and well behaved through the vortex breakdown region and into the large-scale separation portion of the flowfield. Probe A is on the downstream portion of the upper stage. Probes B, C, and D are located on the LVSA. The final port, E, was positioned at the junction between the LVSA and main centerbody.

Transient surface data at each of the five surface locations are shown in Fig. 15 for a simulation that was executed for 10 sec., which is 8 sec. longer than the previously-discussed solution. However, the pressure fluctuations for the baseline solution are plotted between 0 and 2.0 sec. In general, elevated unsteadiness is observed with increased downstream distance. More specifically, minimal fluctuations in C_p exist at Point A, which is on the upper stage. While the asymmetric vortex does cause surface separation, the flow in this region is fairly steady, as previously outlined. As the vortex is shown to breakdown over the LVSA, elevated unsteadiness is observed for the four points on the LVSA. These high-frequency fluctuations are also visible in Fig. 15(c), which shows the deviation (C_p') relative to a mean value. For this analysis, the mean pressure was defined to be the average value over the entire 10 sec. sampling window. Similar to the dimensional time trace, increased unsteadiness is seen with increasing downstream distance.
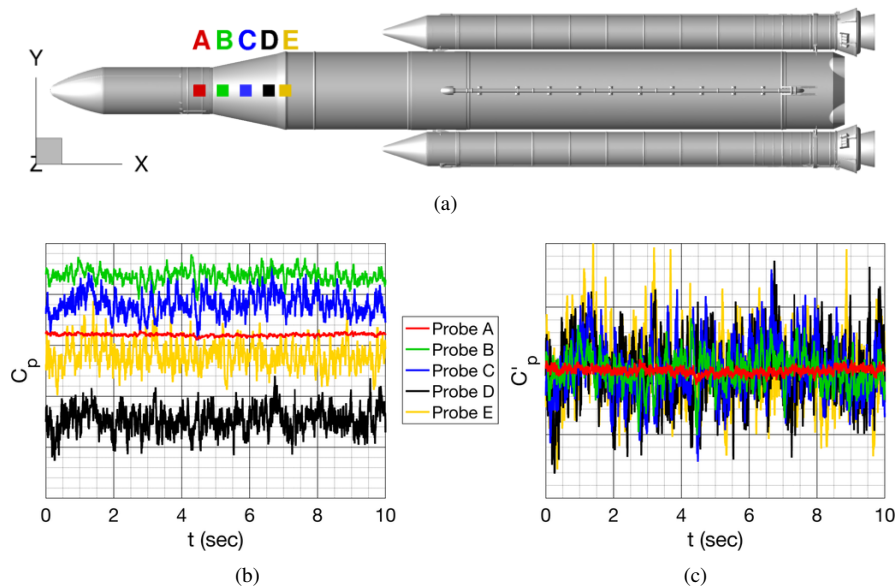

Fig. 15   Transient surface pressure data at a) five locations for b) C_p signal and c) C_p fluctuation relative to time-averaged C_p.

G. Solution at α_T =90 deg.

In addition to considering the grid refinement at α_T =50 deg., a discussion at 90 deg. is also useful. From a mission perspective, this condition corresponds to the vehicle resting on the launchpad and subjected to freestream wind. As the vehicle may be on the launchpad for multiple days, the flowfield and corresponding vehicle behavior on the launchpad is of particular interest. More specifically, the possibility of wind-induced oscillation, resulting from fluid-structure interactions, has the potential to cause damage to the rocket.

A simulation of the isolated vehicle at Mach 0.183 was executed for 26,000 iterations (13 sec.), which is significantly longer than the baseline solution. An extended computation was executed to understand the long-period flowfield behavior. Similar to the previously-discussed solution, the Cartesian grid was refined every 250 iterations based on ω. Seen in Fig. 16(a), significant refinement is applied from iteration 6,000 to 10,000 prior to the total number of points decreasing from a peak of nearly 1.8 billion cells to a stable value near 1.5 billion cells through the time-averaged portion of the solution. A side view of the vehicle depicting the Cartesian grid and solution at iteration 20,000 (10.0 sec.) is plotted in Fig. 16(b) with a slice at y=0 showing the magnitude of vorticity in the flowfield, the variable on which the

grid was refined. A vertical line depicting the slice location for results in Fig. 17, discussed later, is also shown. In the vehicle orientation shown in Fig. 16(b), the freestream flow is oriented from the bottom of the figure toward the top of the image. As clearly depicted with this centerline cut, a coarse grid is present downstream of the portion of the centerbody near the SRBs. This decreased resolution could be a result of one of two reasons. First, it is possible that the flowfield exhibits little aerodynamic complexity at this station. However, it is more likely that a large wake is not adequately resolved at this body station.


(a)

(b)
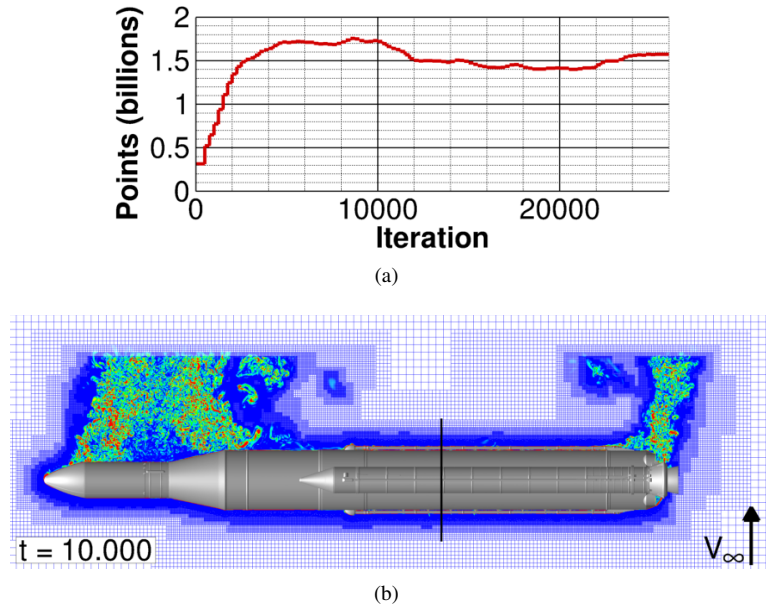
Fig. 16   Cartesian grid refinement during solution at α_T=90 deg. showing a) Cartesian grid size and b) slice colored by ω at the vehicle centerline.

A body station slice was taken through ten different instantaneous solutions, and the results are presented in Fig. 17. Data in the figure are presented from 1.0 sec. through 10.0 sec. The instantaneous time step is shown in the plot for each solution. A body station slice was taken across the SRB at the location indicated by the vertical line in Fig. 16(b). This location was selected such that the flowfield behind the SRBs could be examined in greater detail. It is known that this is one of the most complex portions of the flowfield in discussion. As previously mentioned, the Cartesian grid is initially refined over the first 5.0 sec. prior to coarsening of the grid after that point in time and through the remainder of the solution. Figure 17 clearly shows regions of the flow that are subjected to grid coarsening at increased time steps. More specifically, the separated wake region behind the centerbody may be underresolved later in the solution relative to the region prior to time averaging. Quiescent flow is not expected in this portion of the flowfield. It is possible that the poor resolution in the wake may have an influence on the leeward side of the vehicle and adversely affect the accuracy of the surface solution. While the adaptive mesh refinement is automatically executed within Kestrel, some settings can be adjusted to influence the refinement. A detailed study of the impact of these settings on a case at α_T=90 deg. is beyond the scope of this study, but may be of interest in the future. While data are only shown at one body station, the plots shown are representative of the entire flowfield, including downstream of the region behind the SRBs.

V. Time Step

The fidelity of unsteady global time stepping solutions are affected by the temporal resolution with which the problem is simulated. With a reduction in time step for one given iteration, the fidelity of the solution is increased relative to a larger time step. However, for a given length of physical time in the simulation, a reduction in time step increases the number of iterations for the solution. Consequently, a balance between these two factors must be achieved. In general, the goal is to have a sufficiently-small time step to yield an accurate result without overresolving the temporal regime.

15
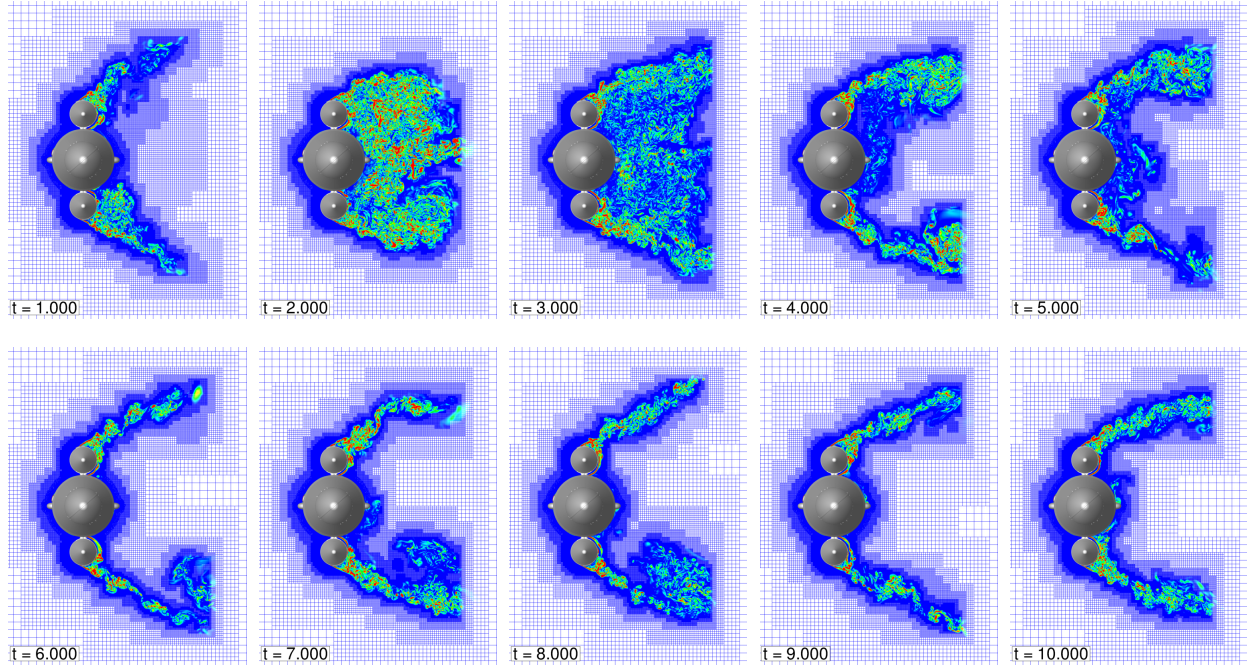
Fig. 17   Slices of ω at x/L=0.35 at α_T=90 deg. showing Cartesian grid refinement through 10.0 sec. of the simulation.

A. Settings

To understand the effect of time step on the solution, nine different time steps were simulated. Relative to a baseline timestep of 0.0005 sec., the tested range of relative time step spanned from 40% to 200%. Table 1 conveys the nine time steps and the relative size to the baseline dt of 0.0005 sec. For all cases listed in the table, the averaging window was selected to be 2.0 sec. To ensure the flow was adequately set up and reached a statistically-steady state, the time-averaging window was defined to begin at 5.0 sec. or 10,000 iterations, whichever was the greater of the two values. These values are listed in the table.

Table 1   Selected Time Steps.

Case	$dt/0.0005$	dt (s)	n_{its}	$n_{avgstart}$	$t_{avgstart}$ (sec.)	t_{total} (sec.)
dt0.4	0.4	0.0002	35,000	25,000	5.0	7.0
dt0.6	0.6	0.0003	23,333	16,667	5.0	7.0
dt0.8	0.8	0.0004	17,500	12,500	5.0	7.0
baseline	1.0	0.0005	14,000	10,000	5.0	7.0
dt1.2	1.2	0.0006	13,333	10,000	6.0	8.0
dt1.4	1.4	0.0007	12,857	10,000	7.0	9.0
dt1.6	1.6	0.0008	12,500	10,000	8.0	10.0
dt1.8	1.8	0.0009	12,222	10,000	9.0	11.0
dt2.0	2.0	0.0010	12,000	10,000	10.0	12.0

B. Convergence

With the near-body and off-body gridding approach, it is necessary to ensure adequate convergence of both the adapted Cartesian grid and the flowfield solution. Prior to the flowfield reaching a statistically-steady state, it is necessary for the grid to reach a nominally unchanging state. Refinement of the Cartesian grid, based on the magnitude of vorticity, occurred over the entirety of the solution, and results for the number of structured blocks and total computational points are shown in Fig. 18. Each time step is presented as a different color with the baseline solution plotted with a black line. The original Cartesian grid, comprised of 315 million cells and nearly 30,000 blocks, was the same for all nine solutions. As seen in the figure, grid convergence is a function of only the iteration number and not of the dimensional solution time. Significant refinement is observed over the first 6,000 iterations with all grids surpassing 1.5 billion cells in this portion of the simulation. After this point, the number of points is relatively independent of time. Ultimately, the grid is comprised of about 65,000 blocks in which the mean block contains about 25,000 cells. As the inputs to the solver for each simulation differed, the final grid for each solution will also be slightly different than the other simulations. However, similar refinement is applied, thus, similar grid sizes and distribution occur.
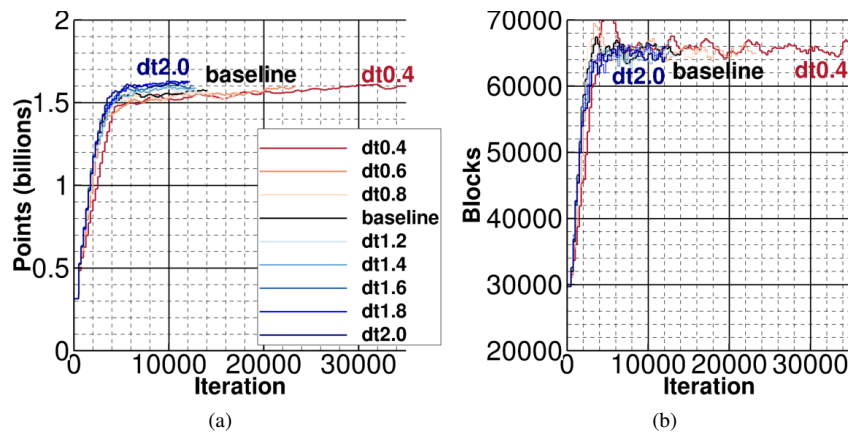

Fig. 18   Cartesian grid refinement for nine time steps quantified by a) number of grid points and b) number of blocks.

Given a sufficient amount of adaptive mesh refinement, it is also important to monitor the solution convergence of forces and and residuals. Figure 19 includes convergence histories for normal force coefficient (C_N), side force coefficient (C_Y), and solution residual. As seen in the figure, the time step has a dramatic effect upon the solution convergence. An increased number of iterations is needed to converge a solution with a reduced time step relative to the baseline case, which is the expected behavior. After a given number of startup iterations, the solutions are observed to converge at different rates relative to the number of iterations. The forces converge most rapidly for larger time steps, and the rate of convergence for decreased time steps is markedly slower. These observations apply to both C_N and C_Y. When analyzing C_N as a function of time, plotted in Fig. 19(c), it is seen that the solutions exhibit similar convergence data as a function of time. This observation indicates that the convergence of the solution is more dependent upon the number of cycles the flow has made through a characteristic length than the number of solution iterations. For all solutions, the slope of convergence is markedly decreased at increased iterations. However, the cases do not approach a flat, statistically-steady state as would be desired. Similar to the baseline solution, this observation indicates the length of the solution and time at which averaging commences should both be increased.

C. Time-Averaged Solution

As previously presented, the time step can have a significant effect upon the final solution including time-averaged and unsteady results. Consider the results in Fig. 20, which shows results at dt=0.0002 sec. (dt0.4), dt=0.0005 sec. (baseline), and dt=0.0010 sec. (dt2.0). In the figure, isosurfaces of constant Q are flooded by the magnitude of vorticity after the 2.0 sec. time-averaging window. In general, minimal changes are observed between the three solutions. While some differences are observed, the topology of the flowfield is relatively consistent. Close examination indicates that the centerbody asymmetric vortices are resolved similarly, and the time step does not affect the x station at which the
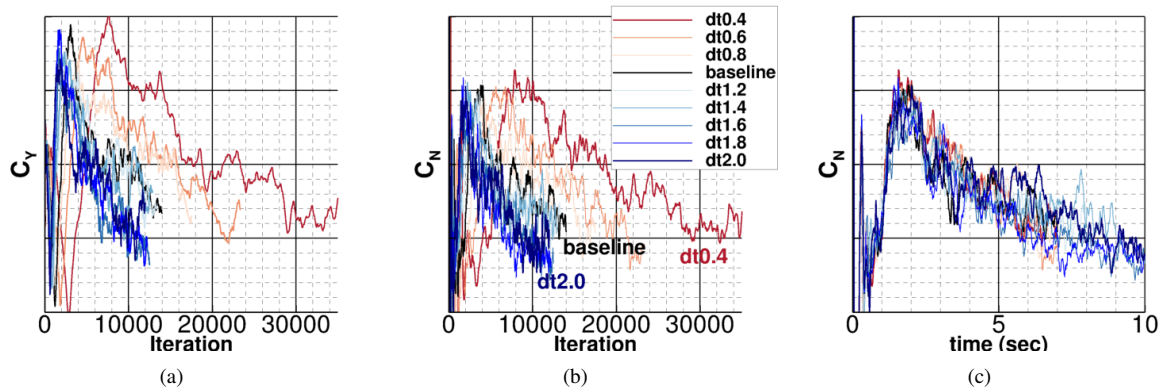
Fig. 19   Effect of time step on flowfield convergence evidenced by a) side force, b) normal force as a function of iteration, and c) normal force as a function of time.

vortices break down into broadband separation. Similarly, the asymmetric vortices on each SRB are extremely similar between all three solutions. Interestingly, some differences are observed in the structure and breakdown of the small vortex emanating from the starboard side of the LVSA. When comparing the two smallest time steps, no significant differences are observed with this vortex. However, the largest time step yields a vortex that breaks down approximately $0.75a$ upstream of the baseline solution. This observation indicates that the larger time step may negatively impact the fidelity of the solution.
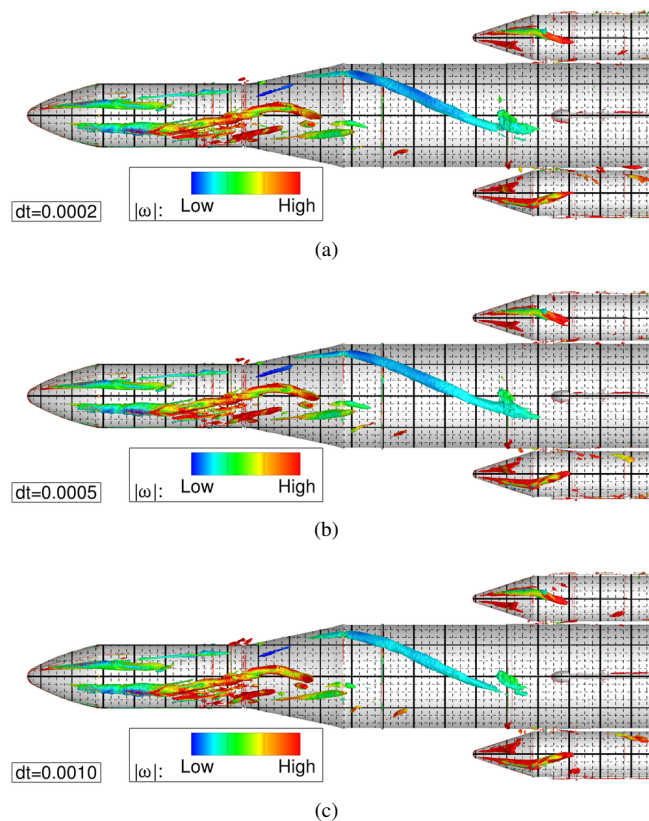

Fig. 20   Isosurfaces of constant Q flooded by $|\omega|$ for a) $dt = 0.0002$, b) $dt = 0.0005$ (baseline) and c) $dt = 0.0010$.

18

In addition to topological flowfield features, the integrated forces applied to the vehicle must be considered. Seen in Fig. 21, both the normal force (C_N) and side force (C_Y) are dependent upon the selected time step. Similar to the baseline case, the normal force is significantly larger than the side force. The normal force is driven by the large, low-pressure region on the leeward side of the vehicle while the side force is caused by the asymmetric vortices and Coandă effect. In general, the forces for $dt<0.0007$ sec. agree reasonably well with each other. However, significant deviations in C_N and C_Y relative to the other values is observed for larger time steps. This conclusion suggests that large time steps, while computationally efficient, may have adverse effects upon the accuracy of the solution. The values in the figure represent the time-averaged solution. For more details on the convergence of the solutions, see Fig. 19 in Sec. V.B.
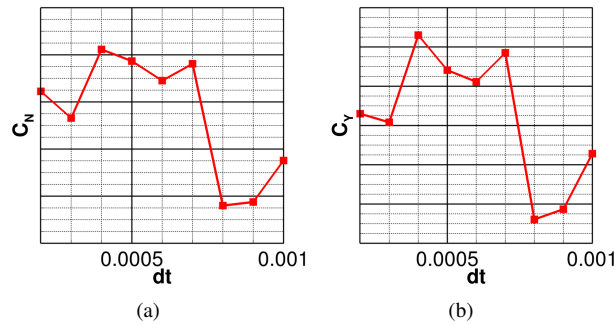
Fig. 21   Forces as a function of time step for a) C_N and b) C_Y.

The lineloads, or longitudinal load distributions, on the vehicle are plotted in Fig. 22, similar to the baseline results shown in Fig. 13. In the figure, data for the centerbody are shown in red, the port SRB data are green, and the starboard SRB data are blue. A shaded, translucent region is bounded by dark, solid lines for each of the three bodies. This shaded region indicates the bound between the minimum and maximum value of the force at a given x station across all nine time steps. No significant trends were observed in which one time step was routinely at or near the outer bounds for a given x station. Excellent agreement between the time steps is observed in regions where the asymmetric vortices dominate the flowfield, both on the centerbody and the two SRBs. In general, less spread is observed for well-behaved portions of the flowfield, which is the expected trend. The large asymmetric vortices on the centerbody result in nonzero side forces over the upper stage and the upstream portion of the center core.
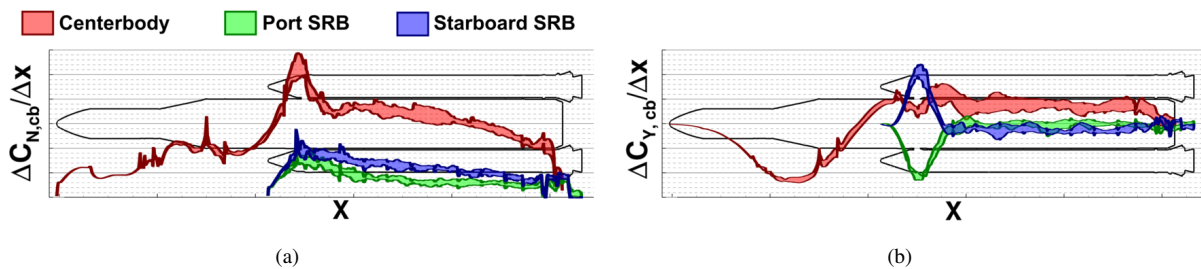
Fig. 22   Minimum and maximum lineloads at a given x station for nine time steps quantified by a) C_N and b) C_Y.

Results indicate that the selected time step affects the solution both on the surface and in the volume. Figure 23 shows the sectional skin friction coefficient over the leeward side of the centerbody and both SRBs at a station cut near the SRB tips. This slice location is indicated by a black vertical line on the vehicle. In general, excellent agreement is observed over all three surfaces across all nine time steps. The asymmetric vortices over the two SRBs result in a complex C_f distribution. On the contrary, the flowfield behind the centerbody, consisting of only a separated wake, does not yield any localized increases or decreases in skin friction. On the port SRB, the inboard asymmetric vortex varies slightly for each time step, as evidenced by the different minimum values of C_f. As no major differences in the

separation patterns over the rocket are observed, it is concluded that the time step does not affect the topology of any flowfield features, as also seen in Fig. 20.

(a)

(b)
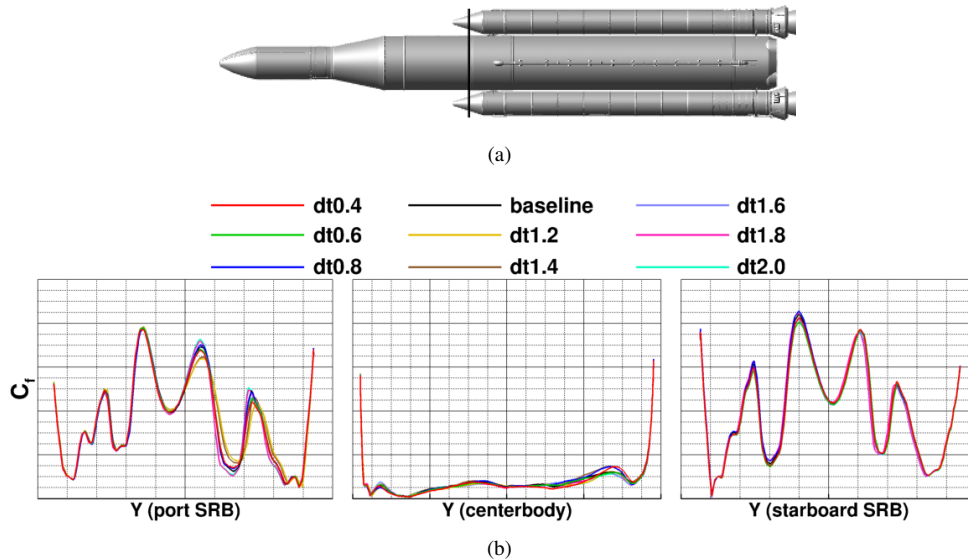
Fig. 23   Sectional slices for nine time steps at a) x **station near tips of SRB showing b)** C_f **on two SRBs and centerbody.**

VI. Turbulence Model

A variety of different turbulence models are implemented in Kestrel, as discussed herein. The one-equation Spalart-Allmaras (SA) turbulence model can be used with or without a rotation correction (RC) or with the additional option to replace the linear Boussinesq approximation with a quadratic constitutive relation (QCR) [31]. Additionally, Menter's two-equation model can be used with or without the shear stress transport (SST) correction [32] and with or without QCR. All of these turbulence models can be used with a steady or unsteady formulation. Each of these models was tested to establish best practices for these SLS simulations.

A. Steady and Unsteady Formulations

The accuracy and fidelity of a flowfield solution, especially one exhibiting massive separation, is very dependent upon the computational formulation, including the selected turbulence model. While Reynolds-averaged Navier Stokes (RANS) and unsteady Reynolds-averaged Navier Stokes (URANS) methods are desirable due to low computational costs, massively-separated flowfields may not be accurately captured with these schemes. Large regions of separation, such as those in this study, may require an unsteady computational formulation, such as detached eddy simulation or large eddy simulations, to yield valid results. While these higher-order methods increase the accuracy of a solution, a marked increase in computational cost is also observed relative to a traditional RANS approach.

The predicted flowfield for Mach 0.183 and α_T of 50 deg. is shown in Fig. 24 for a RANS, URANS, and Improved Delayed Detached Eddy Simulation (IDDES). In the plots, three body station slices are shown and colored by $C_{p,t}$. Dramatic differences between the three simulations are observed. While separation and asymmetric vortices are seen in all three results, the simulations show wildly different behavior around these vortices and in the separated region. Overall, it is seen that both RANS and URANS fail to adequately predict the size and location of the asymmetric vortices and separated region on the leeward side of the vehicle. It is concluded that an unsteady IDDES formulation is needed for this flowfield.
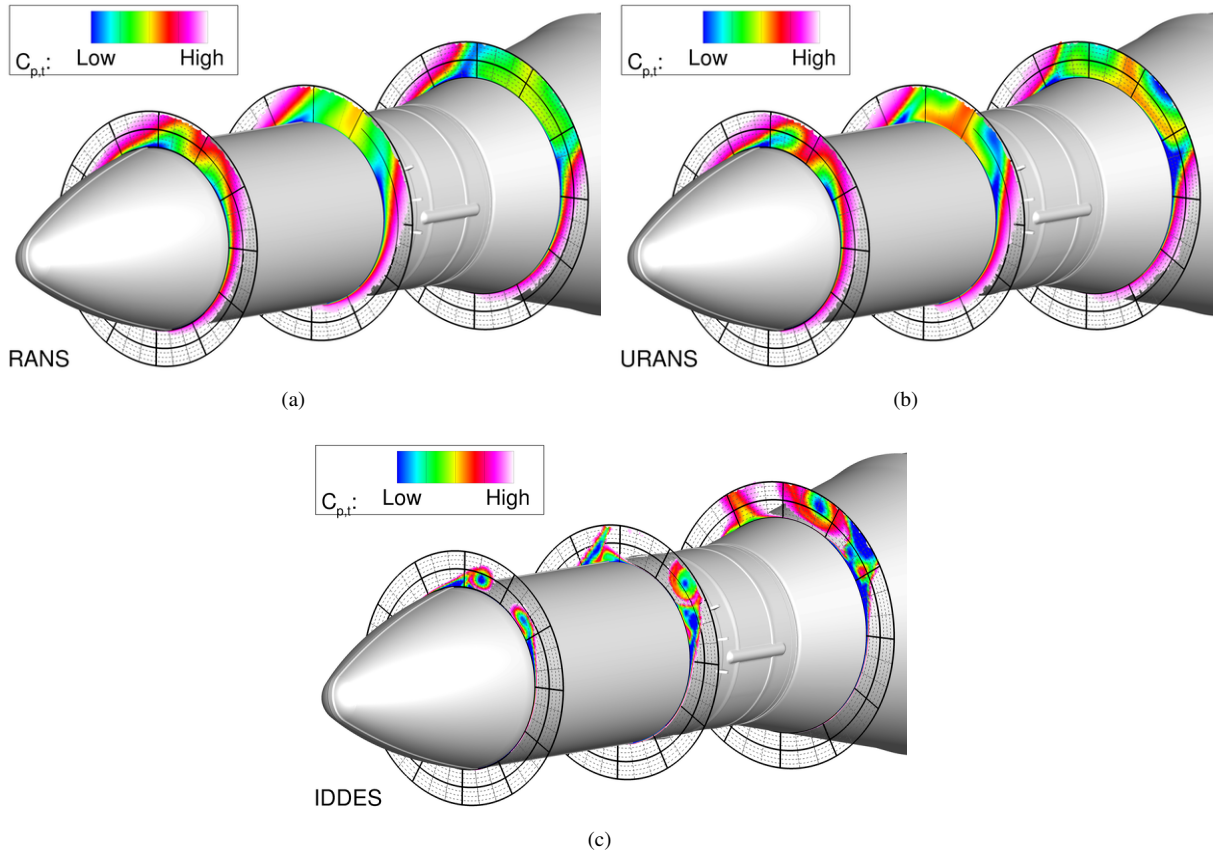
Fig. 24   Isometric view of solution showing three body station slices for a) RANS, b) URANS, and c) IDDES formulations.

B. Volumetric Results

The computed flowfields must be examined in detail if minute differences due to the selection of turbulence model are to be discovered. In particular, it is prudent to compare the turbulence models over the LVSA as this is the region in which the flow decomposes from the stable asymmetric vortices into broadband separation, as seen in Fig. 11. Consider the results plotted in Fig. 25, which show an isocontour of Q that is flooded by $|\omega|$. The results indicate minimal differences in the topological structure of the asymmetric vortices. All three SA models predict a primary asymmetric vortex of similar strength that is nominally aligned with the body centerline. This vortex is seen to burst at similar longitudinal body stations. Careful examination of the results indicates the presence of a secondary vortex in the Menter SST and Menter SST-QCR solutions. This vortex, positioned only slightly to the port side (toward the bottom of the plot) of the primary vortex, is fairly small and compact relative to the primary vortices, as expected.

While Fig. 25 exhibits strong similarities within the SA family of solutions, differences are observed within the Menter family and also when comparing the SA and Menter solutions. First, significant differences are observed between the Menter and both Menter SST variations. In particular, the location of the primary vortex, and also the magnitude of vorticity, varies widely between the cases. The baseline Menter model exhibits a vortex that passes onto the starboard side of the body centerline. Additionally, this vortex is significantly weaker than that of all five other solutions. In general, the Menter SST and Menter SST-QCR models predict elevated values of $|\omega|$ relative to the three SA solutions. Careful examination of all six flowfields suggests additional differences are observed in the small secondary vortex emanating from the upstream edge of the LVSA. Overall, the shape, structure, location, and strength of this vortex varies significantly between the solutions. In particular, it is observed that the secondary vortex breaks down near the most upstream body slice in the Menter SST and Menter SST-QCR models, and all four other models indicate this secondary vortex exists over both body cuts.
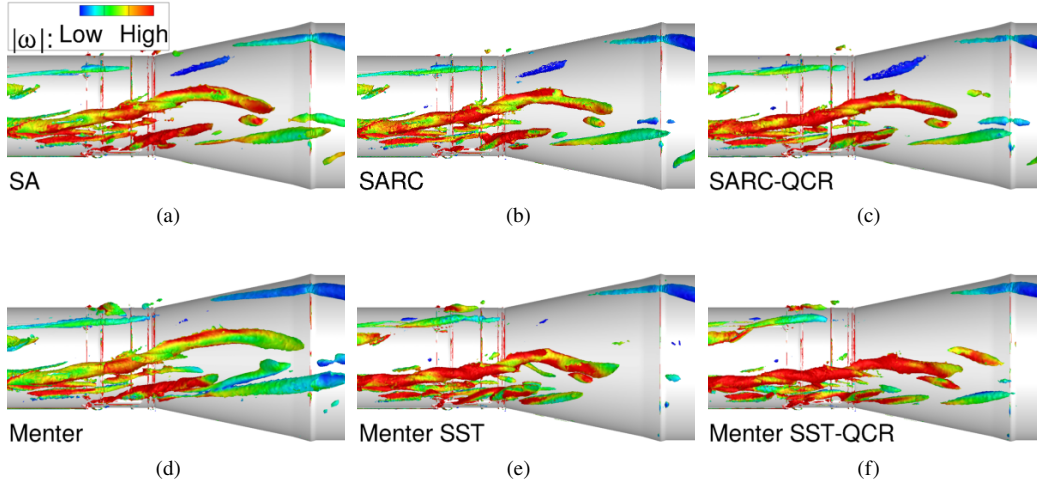
Fig. 25   Leeward side of vehicle showing slice locations and isocontours of constant Q flooded by $|\omega|$ for a) SA, b) SARC, c) SARC-QCR, d) Menter, e) Menter SST, and f) Menter SST-QCR

C. Surface Results

Surface skin friction coefficient data were extracted at two body stations for each of the six solutions, and these results are plotted in Fig. 26. Overall, reasonable agreement is seen when comparing all six solutions over all three surfaces. Near the SRB nose, seen in Fig. 26(b), localized peaks in C_f are caused by the asymmetric vortices. While topologically similar, the computed flowfields do indicate some minor differences at this upstream location, even within the SA or Menter formulations. In particular, the separation pattern is slightly different on the SRBs, most pronounced on the inboard side of the SRBs. On both SRBs, but most notable on the starboard SRB, the Menter model indicates earlier separation relative to all other solutions. Despite these minor differences, the flowfield is similar for all six simulations, indicating the choice of turbulence model does not have a significant effect on the formation of the asymmetric vortices.

Figure 26(c) presents C_f data on the leeward surface near the midpoint of the SRBs. Removed from the influence of asymmetric vortices, the flowfield at this body station is dominated by the separated wake. This station cut was selected such that the Coandă effect and surface separation could be examined. As seen in the figure, both similarities and differences are observed at this downstream slice location for the different models. With the exception of some localized increases in C_f around the leeward LoX line, no local peaks or troughs of C_f are observed.

## VII. Implementation of Best Practices

In addition to the aforementioned time step and turbulence model investigation, ten additional parametric studies were performed to determine the best practices for this analysis. A discussion of each of these sweeps is beyond the scope of this paper but will be presented in a forthcoming NASA Technical Publication. After an exhaustive investigation, it was concluded that nearly all baseline settings were appropriate for this analysis. Analysis of the convergence history indicates that the averaging start window should be later than the baseline simulation, and the solution must be averaged for an increased length of time. It was decided to average the solution for 3.0 sec. (6,000 iterations) starting at 10.0 sec. (20,000 iterations).

Figure 27 depicts the convergence history for the solution with both normal and side force. In each plot, the instantaneous force is depicted as a solid red line. A green line depicts the running average of C_N and C_Y throughout the averaging portion of the solution. A horizontal blue line indicates the value measured in the 14×22 tunnel [8]. Computational data indicate the solution is definitely not settled at iteration 10,000 (5.0 sec.), the start of averaging in the baseline setup. The addition of a significant delay to the start of time averaging allows the flow to set up into an adequately steady state prior to commencing time averaging. While the data suggest a minimum start point could be selected to be as low as 13,000 iterations (6.5 sec.), an extremely conservative value of 20,000 (10.0 sec.) was selected for this simulation. With increasing time, the value of C_N asymptotes to a constant value, indicating an adequately converged solution. As also visualized in the figure, the updated averaging settings improves comparisons to

(a)

(b)

(c)
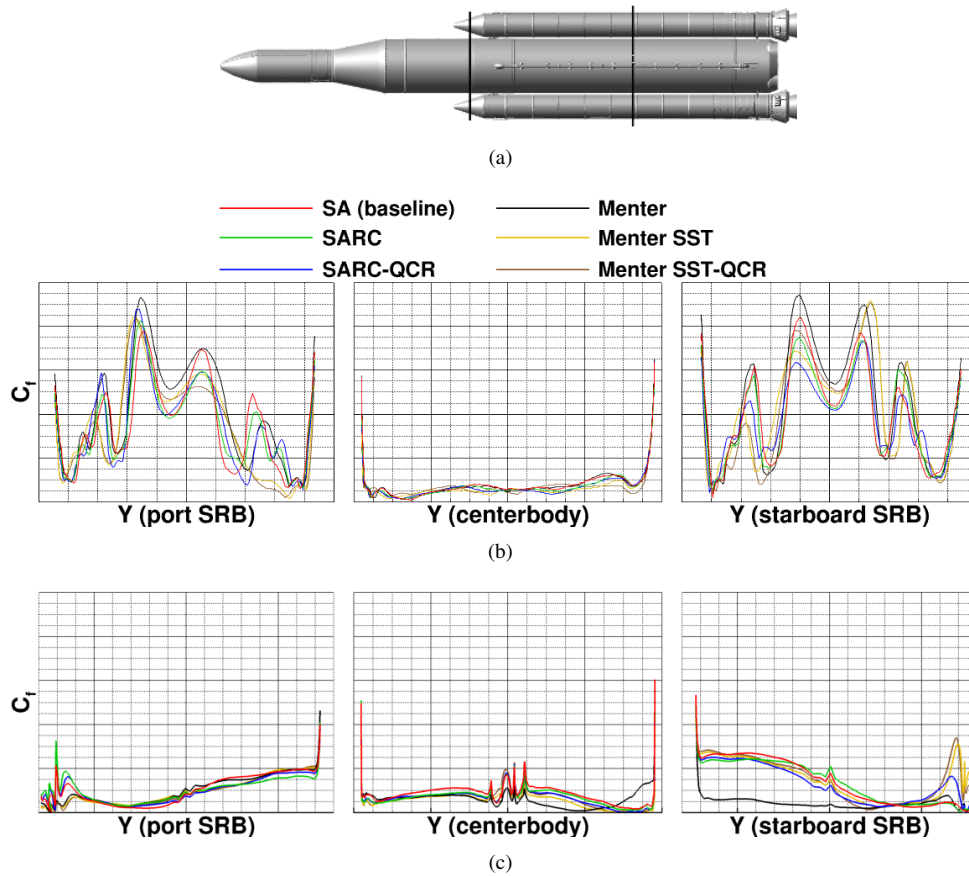
Fig. 26   Sectional slices of C_f for six turbulence models at a) two body stations including b) fore/upstream and c) aft/downstream data.

the experimentally-collected data. Similar to the normal force, the best-practice settings improves the comparison of the side force relative to the normal force.

(a)   (b)
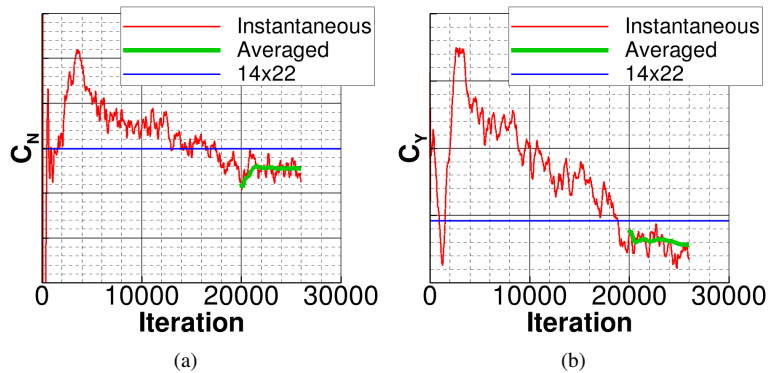
Fig. 27   Integrated force convergence history for improved setup showing instantaneous and time-averaged a) C_N and b) C_Y.

A comparison of best-practice computational data and 14×22 surface pressure results is shown in Fig. 28. The data are presented at three different body stations, as depicted in the figure. Computational data were extracted at the same circumferential points as the instrumented test article. Each of these data points is shown with a small symbol in which red squares and green circles represent the computational and experimental results, respectively. As depicted in Fig. 5, a circumferential ϕ of 0 deg. corresponds to the most downstream point on the launch vehicle, which is nominally opposite the systems tunnel. The core of the model was instrumented with pressure taps at seven body stations comprised of 12 taps per ring. Overall, the two data sets show many similarities at all three plotted body stations. Excellent agreement is found in both the attached and separated regions and this observation is encouraging when considering the degree of separated flow and complexity of the flowfield. It is noted that small differences are observed near ϕ of 90 and 270 deg., which corresponds to the most outward portion of the core that forms the gap. The results in Fig. 28 are representative of all seven pressure cuts. Unfortunately, surface pressure data on the SRBs on the experimental model was not possible as load cells were integrated in the attach hardware, leaving no room for pressure tubes in this hardware or in the interior of the model.
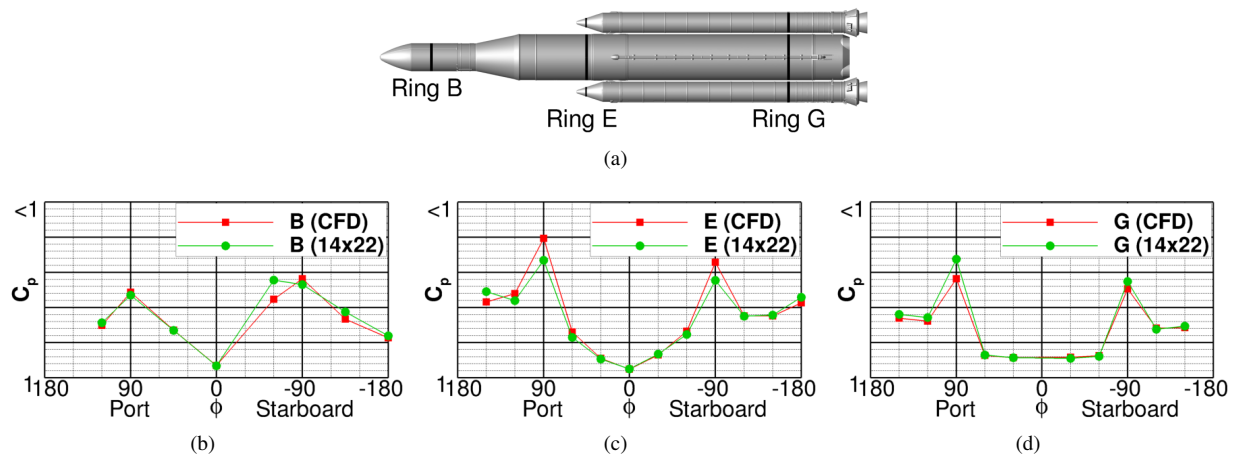
Fig. 28   Experimental (14×22) and computational pressure cuts at a) three body stations including b) Ring B, c) Ring E, and d) Ring G.

VIII. Conclusions and Recommendations

An exhaustive study of the computational methods to predict the SLS in the transition regime of flight was undertaken with Kestrel, a three-dimensional Navier Stokes solver that can implement both RANS and IDDES schemes. The Block 1 Cargo vehicle was studied at Mach 0.183 and α_T =50 deg. As this high-α_T flowfield exhibits significant large-scale separation, both an adaptive mesh routine and unsteady flow solver were needed to accurately predict the wake behind the vehicle. These computational simulations are dependent on the input settings that are used in the program, and it is these settings that is the subject of this paper. In general, the analysis of the baseline setup showed that this approach yielded high-quality results on the surface and in the volume. As found in slender bodies at high angles of attack, two characteristic asymmetric vortices were captured on the upstream portion of both the core and both SRBs. These features were observed in both the instantaneous and time-averaged results.

The effects of both the global time step and turbulence model were also studied in great detail. Nine time steps were simulated that ranged from 40% to 200% relative to the baseline time step. Good agreement was found in the offbody grid refinement, indicating similar grid convergence. The solutions exhibited topological similarities of all global features, such as the asymmetric vortices. Substantiation is also presented that defends the importance of an unsteady IDDES analysis routine to accurately resolve the separated flowfield. Overall, few differences were observed between the models with the exception of the baseline Menter model.

Finally, a set of updated parameters were selected and results were compared to previously-collected experimental data. These data, obtained in the NASA LaRC 14- by 22-Foot Subsonic Tunnel, included both surface pressure distributions as well as integrated force and moment coefficients. Superb agreement was seen in the centerbody surface

pressures on both the windward and leeward side of the vehicle that exhibited attached and separated flow, respectively. The largest deviations, while still small, were observed in the gap between the centerbody and SRBs. No pressure data were collected on the SRBs due to experimental model constraints.

References

[1] NASA, *Artemis Plan: NASA's Lunar Exploration Program Overview*, September 2020.

[2] Blevins, J. A., Campbell Jr., J. R., Bennett, D. W., Rausch, R. D., Gomez, R. J., and Kiris, C. C., "An Overview of the Characterization of the Space Launch System Aerodynamic Environments," AIAA Paper 2014-1253, AIAA Aerospace Sciences Meeting, National Harbor, MD, 2014.

[3] Pinier, J. T., Herron, A. J., and Gomez, R. J., "Advances in the Characterization of NASA's Space Launch System Aerodynamic Environments," AIAA Paper 2019-3397, AIAA AVIATION Forum, Dallas, TX, 2019.

[4] Donahue, B., "Space Launch System: Development Status," AIAA Paper 2016-5415, AIAA SPACE Forum, Long Beach, CA, 2016.

[5] Krist, S. E., Ratnayake, N. A., and Ghaffari, F., "Kestrel Results at Liftoff Conditions for a Space Launch System Configuration in Proximity to the Launch Tower," AIAA Paper 2019-3400, AIAA AVIATION Forum, Dallas, TX, 2019.

[6] Ratnayake, N. A., Krist, S. E., Ghaffari, F., and Deere, K. A., "Computational Fluid Dynamics Methods Used in the Development of the Space Launch System Liftoff and Transition Lineloads Databases," AIAA Paper 2019-3399, AIAA AVIATION Forum, Dallas, TX, 2019.

[7] Wignall, T., "Liftoff and Transition Database Generation for Launch Vehicles Using Data-Fusion-Based Modeling," AIAA Paper 2019-3401, AIAA AVIATION Forum, Dallas, TX, 2019.

[8] Chan, D. T., Paulson Jr., J. W., Shea, P. R., Toro, K. G., Parker, P. A., and Commo, S. A., "Aerodynamic Characterization and Improved Testing Methods for the Space Launch System Liftoff and Transition Environment," AIAA Paper 2019-3398, AIAA AVIATION Forum, Dallas, TX, 2019.

[9] McMillin, S. N., Shea, P. R., Dalle, D. J., Rogers, S. E., Roozeboom, N. H., Meeroff, J. G., and Lee, H. C., "Comparison of Space Launch System Aerodynamic Surface Pressure Measurements from Experimental Testing and CFD," AIAA Paper 2019-3301, AIAA AVIATION Forum, Dallas, TX, 2019.

[10] Ratnayake, N. A., Krist, S. E., Ghaffari, F., and Ahmed, V., "Unstructured Grid Development for the Space Launch System Liftoff and Transition Lineloads Computational Analysis," AIAA Paper 2020-0672, AIAA SciTech Forum, Orlando, FL, 2020.

[11] Pritchett, V., Mayle, M. N., Blevins, J. A., Crosby, W. A., and Purinton, D. C., "Aerodynamic Tests of the Space Launch System for Database Development," AIAA Paper 2014-1256, AIAA Aerospace Sciences Meeting, National Harbor, MD, 2014.

[12] Favaregh, A. L., Houlden, H. P., and Pinier, J. T., "Quantification of the Uncertainties for the Space Launch System Liftoff/Transition and Ascent Databases," AIAA Paper 2016-0795, AIAA Aerospace Sciences Meeting, San Diego, CA, 2016.

[13] Fidler, J., and Bateman, M., "Asymmetric Vortex Effects on Missile Configurations," *Journal of Spacecraft and Rockets*, Vol. 12, No. 11, 1975, pp. 674–681.

[14] Hunt, B., "Asymmetric Vortex Forces and Wakes on Slender Bodies," AIAA Paper 82-1336, AIAA Atmospheric Flight Mechanics Conference, San Diego, CA, 1982.

[15] Degani, D., and Schiff, L. B., "Computation of Turbulent Supersonic Flows Around Pointed Bodies Having Crossflow Separation," *Journal of Computational Physics*, Vol. 66, 1986, pp. 173–196.

[16] Bridges, D. H., "The Asymmetric Vortex Wake Problem - Asking the Right Question," AIAA Paper 2006-3553, AIAA Fluid Dynamics Conference and Exhibit, San Francisco, CA, 2006.

[17] Parks, E., and Peterson, R., "Analysis of a 'Coanda' Type Flow," *AIAA Journal*, Vol. 6, No. 1, 1968, pp. 4–7.

[18] Levinsky, E. S., and Yeh, T. T., "Analytical and Experimental Investigation of Circulation Control by Means of a Turbulent Coanda Jet," Tech. Rep. NASA-CR-2114, 1972.

[19] Morton, S. A., McDaniel, D. R., Sears, D. R., Tillman, B., and Tuckey, T. R., "Kestrel - A Fixed Wing Virtual Aircraft Product of the CREATE Program," AIAA Paper 2009-338, AIAA Aerospace Sciences Meeting, Orlando, FL, 2009.

[20] Morton, S. A., and Meakin, R. L., "HPCMP CREATE-AV Kestrel Architecture, Capabilities, and Long Term Plan for Fixed-Wing Aircraft Simulations," AIAA Paper 2016-0565, AIAA SciTech Forum, San Diego, CA, 2016.

[21] McDaniel, D. R., Tuckey, T. R., and Morton, S. A., "The HPCMP CREATE-AV Kestrel Computational Environment and its Relation to NASA's CFD Vision 2030," AIAA Paper 2017-0813, AIAA SciTech Forum, Grapevine, TX, 2017.

[22] *HPCMP CREATE-AV Kestrel User's Guide*, HPCMP CREATE (Computational Research and Engineering Acquistion Tools and Environments), Air Vehicles, Version 10.3r.

[23] Samareh-Abolhassani, J., "GridTool: A Surface Modeling and Grid Generation Tool," Proceedings of the Workshop on Surface Modeling, Grid Generation, and Related issues in CFD Solutions, NASA CP-3291, 1995.

[24] Frink, N., Pirzadeh, S. Z., Parikh, P. C., Pandya, M. J., and Bhat, M. K., "The NASA Tetrahedral Unstructured Software System (TetrUSS)," *Aeronautical Journal*, Vol. 104, No. 1040, 2000, pp. 491–499.

[25] Krist, S. E., and Ghaffari, F., "Detached Eddy Simulation Results for a Space Launch System Configuration at Liftoff Conditions and Comparison with Experiment," AIAA Paper 2015-0776, AIAA SciTech Forum, Kissimmee, FL, 2015.

[26] Capone, F. J., Paulson Jr., J. W., and Erickson, G. E., "Liftoff and Transition Aerodynamics of the Ares I (A106) Launch Vehicle," AIAA Paper 2011-1253, AIAA Aerospace Sciences Meeting, Orlando, FL, 2011.

[27] Pinier, J. T., Erickson, G. E., Paulson Jr., J. W., Tomek, W. G., Bennett, D. W., and Blevins, J. A., "Space Launch System Liftoff and Transition Aerodynamic Characterization in the NASA Langley 14- by 22-Foot Subsonic Wind Tunnel," AIAA Paper 2015-0775, AIAA SciTech Forum, Kissimmee, FL, 2015.

[28] Shea, P. R., Pinier, J. T., Houlden, H. P., Favaregh, A. L., Hemsch, M. J., Dalle, D. J., Rogers, S. E., Meeroff, J. G., and Lee, H. C., "Ascent Aerodynamic Force and Moment Database Development for the Space Launch System," AIAA Paper 2019-3298, AIAA AVIATION Forum, Dallas, TX, 2019.

[29] Eggert, C. A., Shea, P. R., Ratnayake, N. A., and Krist, S. E., "Effect of Sting Geometry on Axial Force Calculation for the Space Launch System," AIAA Paper 2019-3300, AIAA AVIATION Forum, Dallas, TX, 2019.

[30] Carl L. Gentry, J., Quinto, P. F., Gatlin, G. M., and Applin, Z. T., "The Langley 14-by-22-Foot Subsonic Tunnel: Description Flow Characteristics and Guide for Users," Tech. Rep. NASA-TP-3008, 1990.

[31] Spalart, P., and Allmaras, S., "A One-Equation Turbulence Model for Aerodynamic Flows," AIAA Paper 92-0439, AIAA Aerospace Sciences Meeting and Exhibit, Reno, NV, 1992.

[32] Menter, F., "Zonal Two Equation k-ω Turbulence Models for Aerodynamic Flows," AIAA Paper 93-2906, AIAA Fluid Dynamics Conference, Orlando, FL, 1993.